Lag–luminosity relation in γ-ray burst X-ray flares: a direct link to the prompt emission

R. Margutti,[1,2]⋆ C. Guidorzi,[3] G. Chincarini,[1,2] M. G. Bernardini,[1] F. Genet,[4] J. Mao[1] and F. Pasotti[1]

[1]*INAF Osservatorio Astronomico di Brera, via Bianchi 46, Merate 23807, Italy*
[2]*Physics Department, University of Milano Bicocca, Piazza della Scienza 3, Milano 20126, Italy*
[3]*Physics Department, University of Ferrara, via Saragat 1, I-44122 Ferarra, Italy*
[4]*Racah Institute of Physics, Hebrew University of Jerusalem, Israel*

ABSTRACT

The temporal and spectral analysis of nine bright X-ray flares out of a sample of 113 flares observed by *Swift* reveals that the flare phenomenology is strictly analogous to the prompt γ-ray emission: high-energy flare profiles rise faster, decay faster and peak before the low-energy emission. However, flares and prompt pulses differ in one crucial aspect: flares evolve with time. As time proceeds, flares become wider, with larger peak lag, lower luminosities and softer emission. The flare spectral peak energy $E_{\rm p,i}$ evolves to lower values following an exponential decay which tracks the decay of the flare flux. The two flares with best statistics show higher than expected isotropic energy $E_{\rm iso}$ and peak luminosity $L_{\rm p,iso}$ when compared to the $E_{\rm p,i}$–$E_{\rm iso}$ and $E_{\rm p,i}$–$L_{\rm iso}$ prompt correlations. $E_{\rm p,i}$ is found to correlate with $L_{\rm iso}$ within single flares, giving rise to a time-resolved $E_{\rm p,i}(t)$–$L_{\rm iso}(t)$. Like prompt pulses, flares define a lag–luminosity relation: $L_{\rm p,iso}^{0.3-10\,{\rm keV}} \propto t_{\rm lag}^{-0.95\pm0.23}$. The lag–luminosity is proven to be a fundamental law extending $\sim$5 decades in time and $\sim$5 decades in energy. Moreover, this is direct evidence that γ-ray burst (GRB) X-ray flares and prompt γ-ray pulses are produced by the same mechanism. Finally we establish a flare–afterglow morphology connection: flares are preferentially detected superimposed to one-break or canonical X-ray afterglows.

Key words: radiation mechanisms: non-thermal – gamma-ray burst: general.

1 INTRODUCTION

The high temporal variability was one of the first properties to be attributed to the γ-ray burst (GRB) prompt emission in the γ-ray energy band (Klebsadel, Strong & Olson 1973). The advent of *Swift* (Gehrels et al. 2004) revealed that a highly variable emission characterizes also the early-time X-ray afterglows in the form of erratic flares. This established the temporal variability as one of the key features in interpreting the GRB phenomena.

GRB 050502B and the X-ray flash 050406 (Burrows, Romano & Falcone 2005b; Falcone et al. 2006; Romano et al. 2006b) provided the first examples of dramatic flaring activity superimposed to a smooth decay: in particular, GRB 050502B demonstrated that flares can be considerably energetic, with a 0.3–10 keV energy release comparable to the observed prompt fluence in the 15–150 keV band. Thanks to the rapid repointing *Swift* capability, it was later shown that flares are a common feature of the early X-ray afterglows,

being present in the $\sim$33 per cent of X-ray light curves (Chincarini et al. 2007, hereafter C07; Falcone et al. 2007, hereafter F07). On the contrary, a convincing optical flare, counterpart to a detected X-ray flare, is still lacking, suggesting that the detected optical afterglow contemporaneous to the high-energy flares is dominated by a different emission component [see e.g. GRB 060904B (Klotz et al. 2008), but see also Greiner et al. (2009) where an optical flare was probably detected but, unfortunately, contemporaneous X-ray coverage is lacking].

Based on the temporal and spectral study of a statistical sample of X-ray flares within GRBs, C07 and F07 showed that the flares share common properties and that the flare phenomenology can be described using averaged properties (see C07 and F07, and references therein).

(i) The same GRB can show multiple flares (see e.g. GRB 051117A which contains a minimum of 11 structures in the first 1 ks of observation).

(ii) The underlying continuum is consistent with having the same slope before and after the flare, suggesting that flares constitute a separate component in addition to the observed continuum.

⋆E-mail: raffaella.margutti@brera.inaf.it

(iii) Each flare determines a flux enhancement evaluated at the peak time $\Delta F/F$ between ~ 1 and ~ 1000, with a fluence that competes in some cases (e.g. GRB 050502B) with the prompt γ-ray fluence. The average flare fluence is ~ 10 per cent the 15–150 keV prompt fluence.

(iv) Flares are sharp structures, with $\Delta t/t \sim 0.1$, a fast rise and a slower decay.

(v) Each flare determines a hardening during the rise time and a softening during the decay time (F07), reminiscent of the prompt emission (e.g. Ford et al. 1995): the result is a hardness ratio curve that mimics the flare profile (see e.g. GRB 051117A; Goad et al. 2007, their fig. 9). In this sense flares are spectrally harder than the underlying continuum.

(vi) The spectrum of a consistent fraction of flares is better fitted by a Band (Band et al. 1993) model, similarly to prompt emission pulses (see e.g. Kaneko et al. 2006). The flare spectral peak energy is likely to be in the soft X-ray range (a few keV). The spectrum evolves with time as testified by the hardness ratio curve and by accurate spectral modelling. During the decay time a clear softening is detected (e.g. Krimm et al. 2007; Godet et al. 2007).

(vii) There is no correlation between the number of flares and the number of prompt emission pulses.

(viii) The vast majority of flares are concentrated in the first 1 ks after trigger. However, late-time flares ($t_{\rm peak} \sim 10^5–10^6$ s) are present as well: flares are not confined to the steep decay phase, but can happen during the plateau and the normal decay phases. Their temporal properties are consistent with those of early flares (Curran et al. 2008), even if their lower brightness prevents a detailed comparison with the entire set of early-time flare properties (this is especially true from the spectral point of view).

(ix) Flares happen both in low- and high-z environments: the record holder GRB 090423 at $z \sim 8.2$ (Salvaterra et al. 2009; Tanvir et al. 2009) shows a prominent flare with standard properties when compared to the sample of X-ray flares of Chincarini et al. (2010) (hereafter C10).

(x) Flares have been detected both in hard and soft events such as X-ray flashes (e.g. XRF 050406).

(xi) Variability has also been detected in the X-ray afterglows of *short* GRBs (GRB with a prompt emission duration $T_{90} < 2$ s, Kouveliotou et al. 1993). However, given the lower brightness associated to these events it is still unclear if what is currently identified as a short GRB flare emission quantitatively shares the very same properties as the population of flares detected in *long* GRBs. GRB 050724 (Barthelmy et al. 2005b) constitutes a good example of short GRB with late-time variability.

From the systematic study of 113 flares in the X-ray Telescope (XRT) 0.3–10 keV energy band, as well as in four subenergy bands, C10 demonstrated the following.

(i) Flares are asymmetric with an average asymmetry parameter similar to the prompt emission value; no flare is found rising slower than decaying.

(ii) The flare width evolves linearly with time $w \propto 0.2t_{\rm peak}$. This is a key point which clearly distinguishes the flares from the prompt emission, where no evolution of the pulse width has ever been found (see e.g. Ramirez-Ruiz & Fenimore 2000).

(iii) The width evolution is the result of the linear evolution of both the rise and the decay times: $t_{\rm r} \propto 0.06t_{\rm peak}$; $t_{\rm d} \propto 0.14t_{\rm peak}$.

(iv) The asymmetry does not evolve with time. Instead the rise over decay time ratio is constant with time, implying that both timescales are stretched of the same factor. Furthermore $t_{\rm d} \sim 2t_{\rm r}$. Flares are *self-similar* in time.

(v) At high energy the flares are sharper with shorter duration: $w \propto E^{-0.5}$. Prompt pulses share the same property, with a similar dependence on the energy band (Fenimore et al. 1995; Norris et al. 1996).

(vi) The flare peak luminosity decreases with time. Accounting for the sample variance the best-fitting relation reads $L_{\rm peak} \propto t_{\rm peak}^{-2.7\pm0.5}$. The average flare luminosity declines as a power law in time $\langle L \rangle \propto t^{-1.5}$ (Lazzati, Perna & Begelman 2008).

(vii) The isotropic 0.3–10 keV flare energy distribution is a log-normal peaked at $\sim 10^{51}$ erg (this can be viewed as the typical flare isotropic energy). The distribution further shows a hint of bimodality.

(viii) In multiple-flare GRBs, the flares follow a softening trend which causes later time flares to be softer and softer: the emitting mechanism keeps track of the previous episodes of emission.

Starting from these pieces of evidence, C07, F07 and C10 concluded that in spite of the softness and width evolution, the X-ray flares and the prompt pulses are likely to share a common origin. However, important questions are still to be addressed: do flares follow the entire set of temporal and spectral relations found from the analysis of prompt emission pulses? In particular, is it possible to define a flare peak lag? Do flares follow a lag–luminosity relation? Is the lag time linked to other temporal properties (e.g. the flare duration, asymmetry, etc.)? What can be said about the Pulse Start Conjecture for flares (Hakkila & Nemiroff 2009)? Is it possible to quantify the evolution of the flare temporal properties as a function of the energy band? Do the rise and decay times evolve differently with energy band? Is it possible to track and quantify the evolution of the spectral peak energy $E_{\rm p}$ during the flare emission? Is there any connection between the temporal and spectral properties of the flares? What is the position and the track of the flares in the $E_{\rm p}$–$L_{\rm iso}$ (spectral peak energy–isotropic luminosity) plane? Is there any link between the flares and the underlying X-ray afterglow morphology?

This set of still open questions constitutes the major motivation for undertaking the present investigation. The primary goal of this paper is to model the X-ray flare profiles and constrain their evolution with energy to obtain parameters that uniquely qualify the shape and spectrum of the flares and compare those values to the well-known signatures of the prompt emission pulses. Since this is often difficult because of low statistics, overlap or non-trivial estimate of the underlying continuum, this paper concentrates on very bright and isolated flares for which the underlying continuum does not play a major role neither from the temporal point of view nor from the spectral point of view. This paper is observationally driven: a critical review of theoretical models in the light of the present results is in preparation.

This paper is organized as follows. The sample selection and data reduction are described in Section 2. In Section 3 we perform the flare temporal analysis, while Section 4 is dedicated to the spectral properties of the sample. The discussion follows (Section 5). Conclusions are drawn in Section 6.

The phenomenology of the different GRBs is presented in the observer frame unless otherwise stated. The 0.3–10 keV energy band is adopted unless specified. The zero time is assumed to be the trigger time. The convention $F(\nu, t) \propto \nu^{-\beta}t^{-\alpha}$ is followed, where β is the spectral index, related to the photon index Γ by $\Gamma = \beta + 1$. All the quoted uncertainties are given at 68 per cent confidence level (CL): a warning is added if it is not the case. Standard cosmological quantities have been adopted: $H_0 = 70\,{\rm km\,s^{-1}\,Mpc^{-1}}$, $\Omega_\Lambda = 0.7$, $\Omega_{\rm M} = 0.3$.

2 SAMPLE SELECTION AND DATA REDUCTION

We select the brightest, isolated flares detected by the XRT (Burrows et al. 2005a) on board *Swift* (Gehrels et al. 2004) in the time period 2005 April to 2010 January. The sample comprises nine flares detected in eight different GRBs[1]: GRB 050822, GRB 060418, GRB 060526, GRB 060904B, GRB 060929, GRB 070520B, GRB 070704 and GRB 090621A[2] (see Table A1). The required isolation allows us to constrain the flares' temporal and spectral properties with high accuracy; their brightness assures the possibility to analyse in detail the evolution of their temporal properties in different energy bands inside the 0.3–10 keV of the XRT; at the same time, this requirement guarantees that the partial ignorance of the underlying continuum properties has a negligible impact on our conclusions, both from the spectral and from the temporal point of view.

XRT data have been processed with the HEASOFT package v. 6.6.1 and corresponding calibration files: standard filtering and screening criteria have been applied. *Swift*-XRT is designed to acquire data using different observing modes to minimize the presence of pile-up. When the source is brighter than a few count s^{-1}, the data are acquired in Windowed Timing (WT) mode. In this case we applied the standard pile-up corrections following the prescriptions of Romano et al. (2006a) when necessary. For lower count rates the spacecraft automatically switches to the Photon Counting (PC) mode to follow the fading of the source. The events are extracted from circular regions centred at the afterglow position with progressively smaller radii to assure the best signal-to-noise ratio (S/N). When the PC data suffered from pile-up, we extracted the source events in an annulus whose inner radius is derived comparing the observed to the nominal point spread function (PSF; Moretti et al. 2005; Vaughan et al. 2006). The background is estimated from a source-free portion of the sky and then subtracted. The background-subtracted, PSF and vignetting-corrected light curves were then rebinned so as to assure a minimum S/N equals to 4 for WT and PC mode data. Data coming from different orbits of observation were merged to build a unique data point, when necessary. This procedure was applied to extract GRB light curves in the nominal XRT energy range (0.3–10 keV) as well as count-rate light curves of the same event in four different subenergy bands: 0.3–1, 1–2, 2–3 and 3–10 keV.[3]

3 FLARE TEMPORAL ANALYSIS

Each flare profile in each energy band is modelled using the Norris et al. (2005) (hereafter N05) profile. This choice allows a direct comparison between the properties of the X-ray flares and of the wide, long-lag prompt pulses analysed by N05 (see Section 5). The N05 profile reads:

$$I(t) = A\lambda \exp\left[-\frac{\tau_1}{(t - t_s)} - \frac{(t - t_s)}{\tau_2}\right] \quad \text{for } t > t_s, \quad (1)$$

where $\lambda = \exp(2\mu)$ and $\mu = (\tau_1/\tau_2)^{1/2}$. t_s is the pulse onset time. The parameters are defined following N05. In particular, the intensity peaks at

$$t_{\text{peak}} = t_s + (\tau_1\tau_2)^{1/2}. \quad (2)$$

The pulse width is measured between the two $1/e$ intensity points and consequently reads

$$w = \tau_2(1 + 4\mu)^{1/2} = t_r + t_d. \quad (3)$$

The asymmetry is defined as

$$k = (1 + 4\mu)^{-1/2} = \frac{t_d - t_r}{t_d + t_r}, \quad (4)$$

where t_d and t_r are the $1/e$ decaying and rising times, respectively:

$$t_{d,r} = \frac{1}{2}\tau_2[(1 + 4\mu)^{1/2} \pm 1]. \quad (5)$$

We account for the entire covariance matrix during the error propagation procedure. The continuum underlying the flare emission is estimated from data acquired before and after the flare and is modelled using a power law or a broken power law: the parameters related to the continuum have been left free to vary in a first fit and then frozen to their best-fitting values in a second fit. The best-fitting parameters and related quantities are reported in Table A1. Fig. 1 shows the best-fitting profiles in the different XRT bandpasses obtained for the flare detected in GRB 060904B, taken as an example. A general trend can be seen for the flare to be wider and peak later at lower energies. A complete summary of the results obtained from the fitting procedure in different energy bands is portrayed in Fig. 2: the detected evolution of the different parameters with energy (panels f to m) will be extensively treated in Sections 3.2 and 3.3. The flare detected in GRB 060904B is here shown as an example.
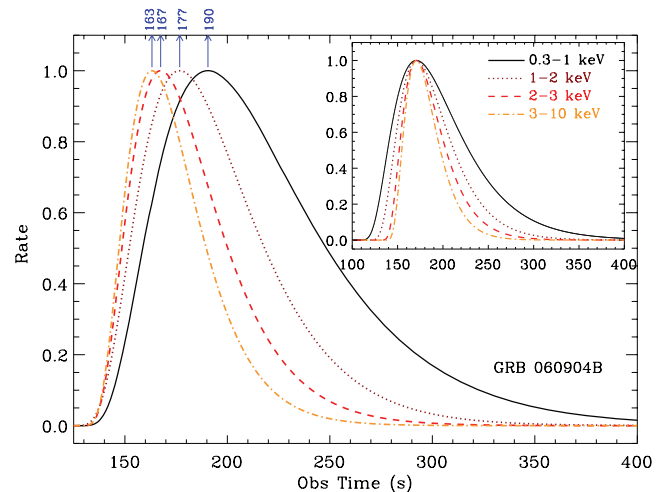
Figure 1. Best-fitting profile of the flare detected in GRB 060904B in different XRT energy bands. The thick line, dotted line, dashed line and dot–dashed line refer to the flare profile observed in the 0.3–1, 1–2, 2–3 and 3–10 keV energy bands, respectively. The profiles have been renormalized for the sake of clarity. The blue arrows point to the flare peak times in the different energy bands. Softer energy band profiles peak later. Inset: the renormalized best-fitting profiles have been aligned at $t_{\text{peak}} = 170.71$ s, peak time of the flare in the 0.3–10 keV energy band as derived from the best-fitting parameters of Table A1. Softest profiles are wider.

---

[1] GRB 050502B is not included since the bright flare detected by the XRT is possibly due to the superposition of more than one structure (Burrows et al. 2005b; C10).

[2] Note that for GRB 090621A, the Burst Alert Telescope (BAT; Barthelmy et al. 2005a) triggered on the precursor (Curran et al. 2009).

[3] Note that differently from C10 the described data reduction assures a minimum S/N equal to 4 for *each* data point of the GRB light curves in the different energy bands. This allows a higher sensitivity which translates into a more accurate evaluation of the best-fitting parameters.

Figure 2. Panels (a) through (e): GRB 060904B flare best-fitting profile in the total 0.3–10 keV XRT energy band and in the four channels. Insets: BAT signal contemporaneous to the flare emission detected in the 15–150, 15–25, 25–50, 50–100 and 100–150 keV energy bands. The typical uncertainty affecting the BAT data is also shown. Panels (f) through (m): observed evolution of the flare decay time (f), rise time (g), width (h), asymmetry (i), start time (l) and peak time (m) with observed energy band. The best-fitting power-law relation describing the evolution of each parameter is drawn with a red solid line and explicitly written in each panel. The fit reported in panel (m) concerns the XRT data only.
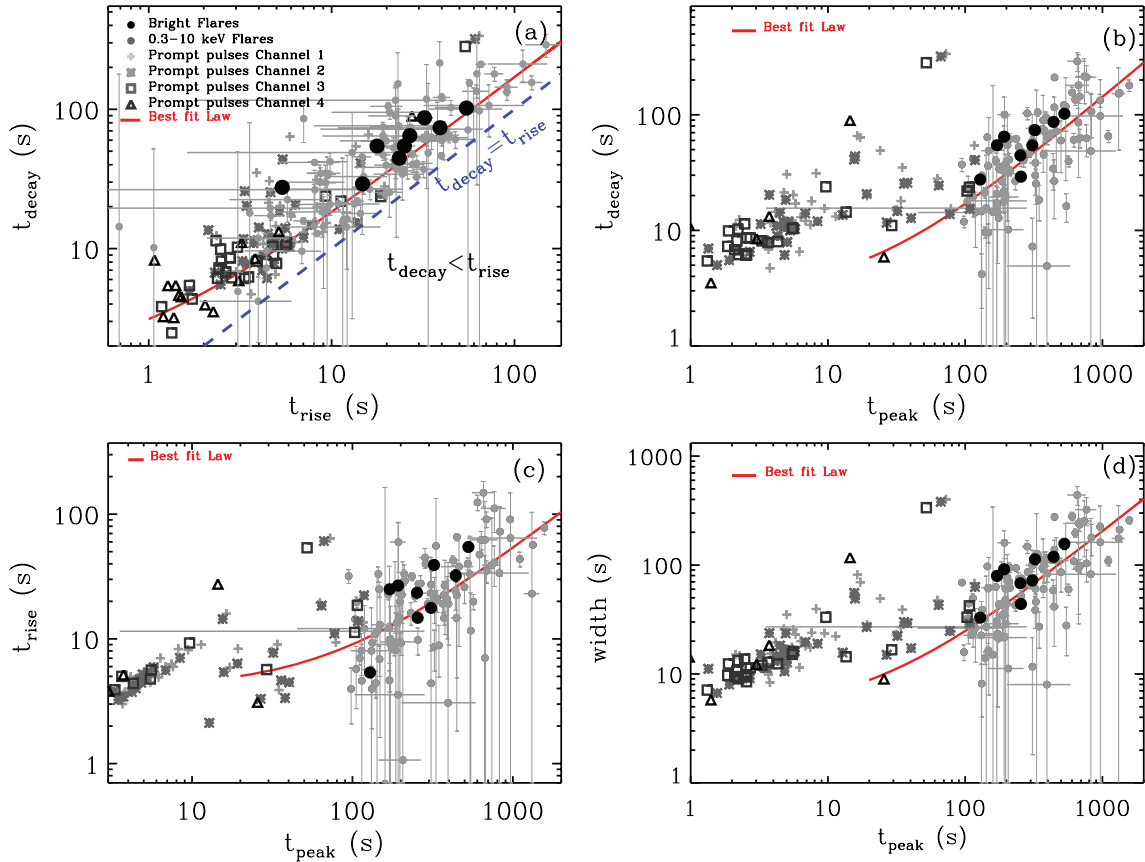
Figure 3. Scatter plot of the temporal parameters describing the flare profile as derived from the best-fitting values reported in Table A1. (a) Decay versus rise time for our sample of bright flares (black dots), for the sample of flares analysed by C10 (grey dots) compared to the values found by N05 for a sample of long-lag, wide prompt pulses detected by BATSE. Blue dashed line: locus of the points for which $t_r = t_d$. Red solid line: best-fitting law for the three samples: $t_d = (1.1 \pm 0.1) + (1.9 \pm 0.1)t_r$. (b) Decay versus peak time for the three samples described for panel (a). Red solid line: linear best-fitting relation found for the flare samples: $t_d = (3.0 \pm 0.4) + (0.14 \pm 0.02)t_{peak}$. (c) Rise versus peak time. The best-fitting relation found for flares is marked with a red solid line: $t_r = (4.0 \pm 0.3) + (0.06 \pm 0.01)t_{peak}$. (d) Width versus peak time. Red solid line: flare best-fitting relation: $w = (4.8 \pm 0.6) + (0.20 \pm 0.02)t_{peak}$.

3.1 Best-fitting parameter correlations

Figs 3 and 4 show the correlations or the lack thereof, for the quantities derived from the best-fitting parameters of Table A1 superimposed to the results obtained by N05 for a sample of long-lag wide prompt GRB pulses and by C10 for a sample of 113 early X-ray flares. In these plots we see that bright flares obey the set of correlations found for the complete X-ray flare catalogue: the rise time is linearly correlated with the decay time, and both linearly evolve with time. This gives rise to a flare width that linearly grows with time (see Fig. 3).

Fig. 4 depicts instead the relation between the asymmetry k and the temporal parameters describing the flare profiles and demonstrates that it is not possible to distinguish the bright from the main sample on the basis of their asymmetry. Furthermore, the asymmetry seems to be independent of the other parameters (Fig. 4).

3.2 Best-fitting parameter evolution with energy

The well-known trend of narrower pulses at higher energy is apparent in Fig. 1 for the flare detected in GRB 060904B. This trend is quantified in Fig. 5 for the entire sample: the narrowing with energy

follows a power-law behaviour[4]: $w \propto E^{-0.32\pm0.01}$. The same is true for the rise and decay times: $t_r \propto E^{-0.37\pm0.01}$; $t_d \propto E^{-0.29\pm0.01}$. The width evolution is the combined result of the evolution of these two time-scales and its evolution is consequently associated to a power-law index which is between 0.29 and 0.37. Notably the rise time shows a steeper dependence on the energy band than the decay time (Fig. 6). As a result, the asymmetry is slightly dependent on energy: flares are on average more asymmetric at higher energies. Flare profiles peak later at lower energies (Fig. 2, panel m); on the contrary, it seems that high-energy profiles start their rise later (Fig. 2, panel l): while the flare in GRB 060904B is here portrayed as an example, the same is true for the entire sample as testified by the results of Table 1.

Fig. 5 also demonstrates that the energy dependence of the various parameters varies from one flare to another: the average relations

---

[4] For the 0.3–1, 1–2 and 2–3 keV energy bands, we define an effective energy $E_{eff} = \frac{\int_{E_2}^{E_1} E f(E) \mathrm{RM}(E)\mathrm{d}(E)}{\int_{E_2}^{E_1} f(E)\mathrm{RM}(E)\mathrm{d}(E)}$ where RM stands for the XRT response matrix, $f(E) \sim E^{-1}$, as found by C10 for the average flare spectral energy distribution. For the hardest band the best-fitting spectrum of each flare is used.
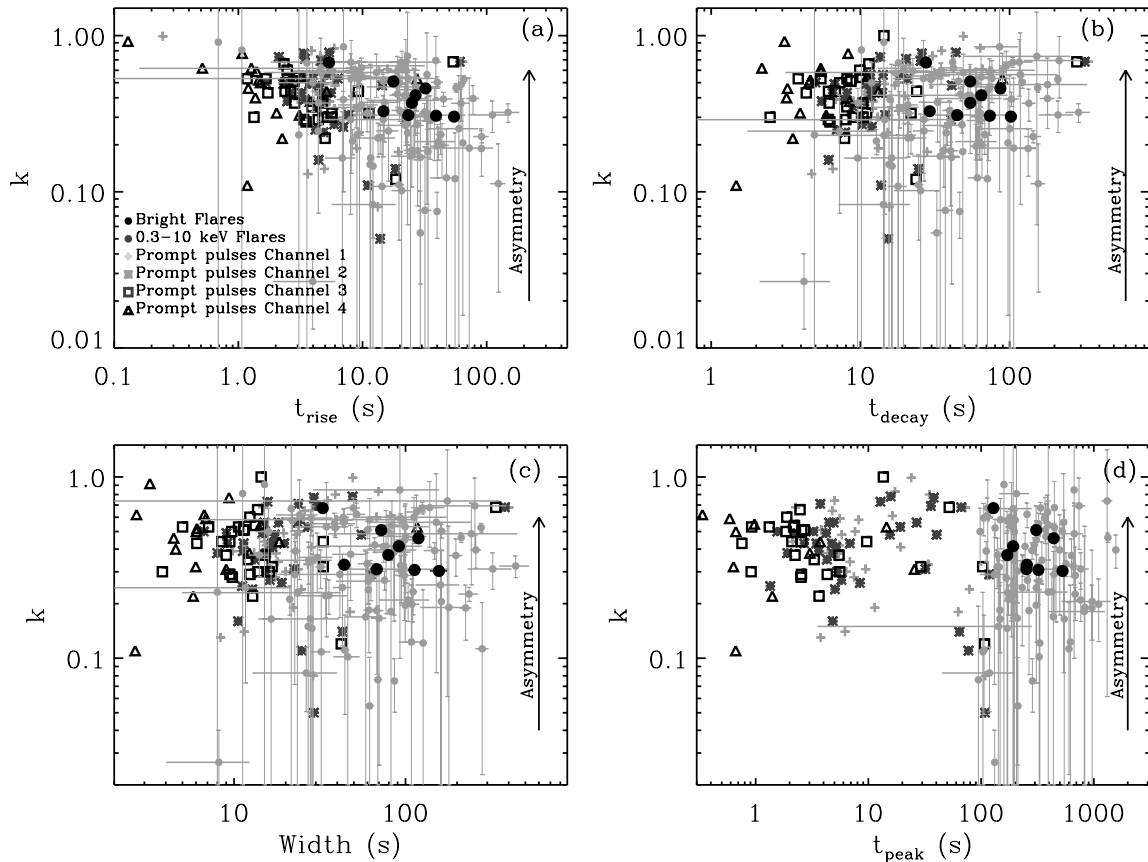
Figure 4. Asymmetry versus rise time (panel a), decay time (panel b), width (panel c) and peak time (panel d) for our sample of bright X-ray flares (black dots), the sample of flares from C10 (grey dots) and for a sample of long-lag, wide prompt pulses from N05. In each plot, the arrow points to the direction of growing asymmetry.

describe the general behaviour of the parameters with energy band, but the evolution in a particular flare can be markedly different. This statement is quantified in Table 1, where the best-fitting power-law index describing the behaviour of the temporal parameters with energy band is listed. The best-fitting relations are portrayed in Fig. 2 (panels f through m) for GRB 060904B. How this different evolution rate relates to the spectral properties of the flares is investigated in Section 4.

3.3 Pulse peak lag

A commonly used parameter related to the spectral evolution of the pulses is the time lag between two energy channels. In this paper we always refer to the flare *peak lag* which is defined as the difference between the peak of the lowest and highest energy profiles measured by the XRT as derived from the best-fitting parameters of Table A1. Taking the flare detected in GRB 060904B as an example, from Fig. 1 a clear tendency is apparent for the peak in the harder channel to lead that in the softer channel: this translates into a measurable positive pulse peak lag. The same is true for the entire sample of flares. The evolution of the flare peak times as a function of energy in the XRT bandpass is reasonably well represented by a power law, as testified by Table 1 and by Fig. 2. Again, different flares have different rates of evolution of their peak times in fixed energy bandpasses.

We scanned the BAT data looking for detections of the bright flares in the 15–150 keV energy range: a peak-finding algorithm is

run. The software is written to automatically scan the observations using all the possible rebinning time-scales: the central time of the bin which maximizes the detection is used as flare peak time. The flare peak times in the γ-ray band have been added to Fig. 2, panel m, when a 5σ detection was found. As appears from this figure, the flare peaks at high energy are not consistent with the extrapolation of the law deduced from X-ray data alone. The same is true for the flares in GRB 060418, GRB 060526 and GRB 070704 which have a BAT detection contemporaneous to the flare emission. With reference to GRB 060904B, it is notable that the highest rate of evolution of t_{peak} is found for bandpasses which are crossed by the spectral peak energy E_{p} during the flare emission (see Section 4.3).

The presence of correlations between the peak lag and the flare-shape parameters is investigated in Fig. 7. The lag is found to be positively correlated with both the rise and the decay times (panel a), giving rise to the width–lag correlation portrayed in panel (b): the wider the flare, the higher the lag value. The same is true for the flare peak time: later flares are associated to larger time lags.

4 FLARE SPECTRAL ANALYSIS

The flare emission has been proven to undergo a strong spectral evolution with the hardness ratio tracking the flare profile (see e.g. Goad et al. 2007). This results in flare profiles on average harder than the underlying continuum. In this section we quantify the spectral properties of each flare of our sample using the hardness ratio analysis (Section 4.1). A link between the temporal and spectral properties is
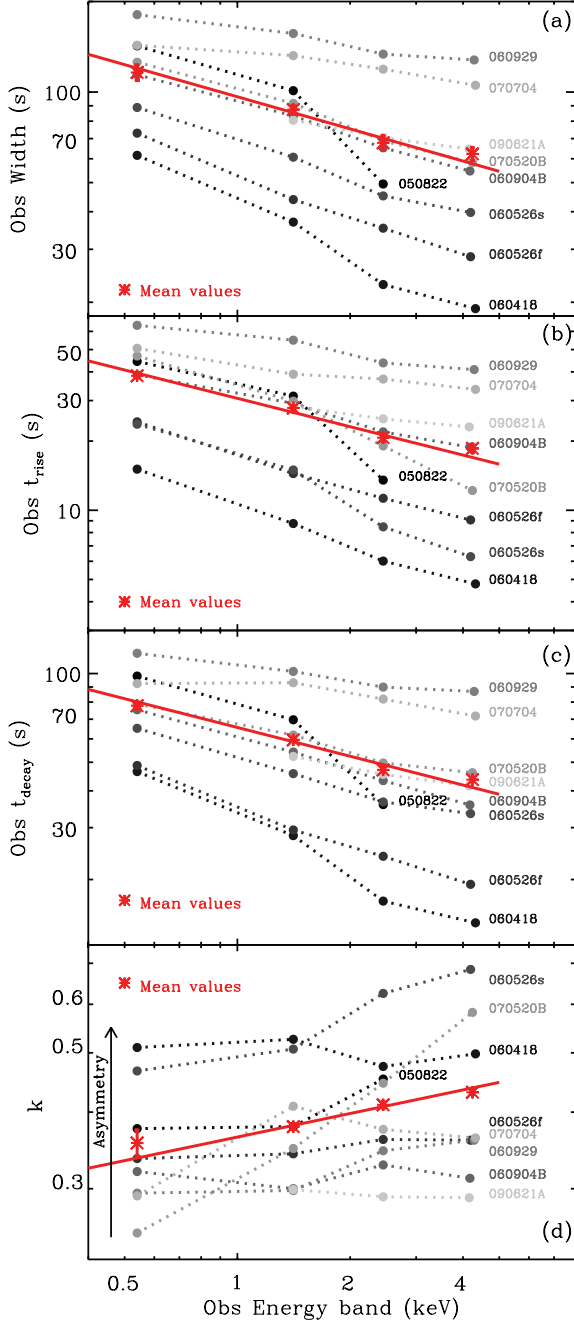
Figure 6. Best-fitting power-law index describing the evolution of the decay time with observed energy as a function of the best-fitting power-law index found for the evolution of the rise time with energy. Red dashed line: locus of the points for which $\alpha_{td} = \alpha_{tr}$. Darker points are associated to spectrally harder flares.

in the time interval t_i through t_f, where $t_i = t_{peak} - t_r$ and $t_f = t_{peak} + t_d$. t_{peak}, t_r and t_d are derived from the best-fitting parameters of the 0.3–10 keV profile:

$$HR_{tot} = \left.\frac{\text{Counts (2–10 keV)}}{\text{Counts (0.3–2 keV)}}\right|_{t_i}^{t_f}. \qquad (6)$$

During the rise and the decay of each flare, the hardness ratio is defined as follows:

$$HR_{rise} = \left.\frac{\text{Counts (2–10 keV)}}{\text{Counts (0.3–2 keV)}}\right|_{t_i}^{t_{peak}} \qquad (7)$$

and

$$HR_{decay} = \left.\frac{\text{Counts (2–10 keV)}}{\text{Counts (0.3–2 keV)}}\right|_{t_{peak}}^{t_f}. \qquad (8)$$

Fig. 8 clearly shows that flares are harder during the rise time and softer during the decay time. The inset of this figure illustrates the presence of a trend: the harder the overall profile, the lower is the spectral ratio between the rise and the decay portions of a flare. A lower degree of spectral evolution is detected for spectrally harder flares, in agreement with the findings of Section 4.2. Note however that the *difference* between the HR_{rise} and HR_{decay} is higher for harder HR_{tot}.

The connection between the temporal and spectral properties is made in Fig. 9. Panel (c) clearly shows that hard flares are less asymmetric.

4.2 Rate of evolution of a flare profile with energy versus HR

The inset of Fig. 8 suggests the presence of a correlation between the flare observed spectral evolution and the overall spectral hardness: harder flares show a limited level of detected spectral evolution. In this subsection we prove that a similar conclusion is reached through the analysis of the rate of evolution of the temporal parameters describing the flare profiles.

The evolution with energy of each flare profile has been analysed in Section 3.2 parametrizing the evolution of each flare-shape parameter (rise time, decay time, peak time, width and asymmetry) using a power-law model. The best-fitting power-law indices are reported in Table 1 and used as evolution indicators in Fig. 10. This figure clearly shows that the rate of variation of a flare temporal profile is a function of the detected hardness of the emission: the harder

Figure 5. Evolution of the width (a), rise time (b), decay time (c) and asymmetry (d) with observed energy band obtained for our sample of bright X-ray flares. Results coming from the fit of a particular flare in different energy bands are indicated by dots and linked by a dotted line. Red stars: mean values derived from the entire sample. Red solid line: best-fitting power-law model: (a) $w = 10^{1.98 \pm 0.01} E^{-0.32 \pm 0.01}$; (b) $t_r = 10^{1.48 \pm 0.01} E^{-0.37 \pm 0.01}$; (c) $t_d = 10^{1.81 \pm 0.01} E^{-0.29 \pm 0.01}$; (d) $k = 10^{-0.44 \pm 0.01} E^{0.11 \pm 0.01}$.

established in Section 4.2, while a proper spectral modelling is performed for the two flares with the best statistics, measured redshift and BAT detection in Section 4.3.

4.1 Hardness ratio analysis

We define the total hardness ratio as the ratio between the reconstructed counts in the 0.3–2 and 2–10 keV energy bands, calculated
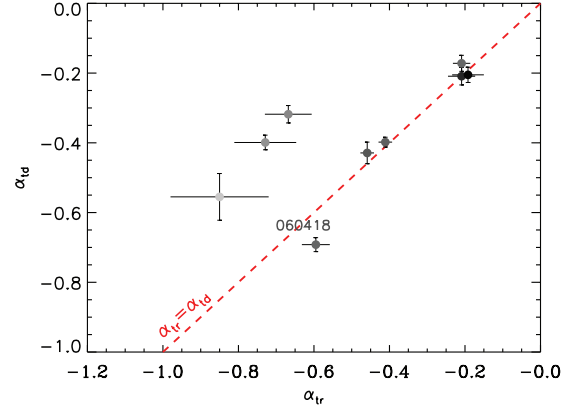
Table 1. Evolution of the flare profile with energy band. The rise time, decay time, peak time, width and asymmetry have been fitted using a power-law model in energy: $y \propto E^{\alpha}$. From left- to right-hand side: power-law index associated to the evolution of the following parameters: rise time α_{tr}, decay time α_{td}, peak time α_{tp}, width α_{w} and asymmetry α_k.

GRB	α_{tr}	α_{td}	α_{tp}	α_{w}	α_k
050822	-0.85 ± 0.13	-0.56 ± 0.07	-0.11 ± 0.03	-0.83 ± 0.10	0.12 ± 0.04
060418	-0.60 ± 0.04	-0.69 ± 0.02	-0.021 ± 0.005	-0.68 ± 0.02	-0.034 ± 0.009
060526f[a]	-0.46 ± 0.02	-0.43 ± 0.03	-0.029 ± 0.001	-0.44 ± 0.02	0.040 ± 0.005
060526s[b]	-0.73 ± 0.08	-0.40 ± 0.02	-0.042 ± 0.006	-0.43 ± 0.01	0.24 ± 0.01
060904B	-0.41 ± 0.02	-0.40 ± 0.02	-0.090 ± 0.014	-0.41 ± 0.06	0.0060 ± 0.039
060929	-0.21 ± 0.02	-0.17 ± 0.02	-0.050 ± 0.006	-0.20 ± 0.04	0.090 ± 0.018
070520B	-0.67 ± 0.06	-0.32 ± 0.03	-0.063 ± 0.025	-0.41 ± 0.07	0.48 ± 0.05
070704	-0.21 ± 0.04	-0.21 ± 0.03	-0.033 ± 0.011	-0.18 ± 0.04	0.039 ± 0.021
090621A	-0.19 ± 0.04	-0.21 ± 0.02	-0.029 ± 0.021	-0.21 ± 0.18	-0.028 ± 0.057

[a]First flare detected by the XRT.
[b]Second flare detected by the XRT.
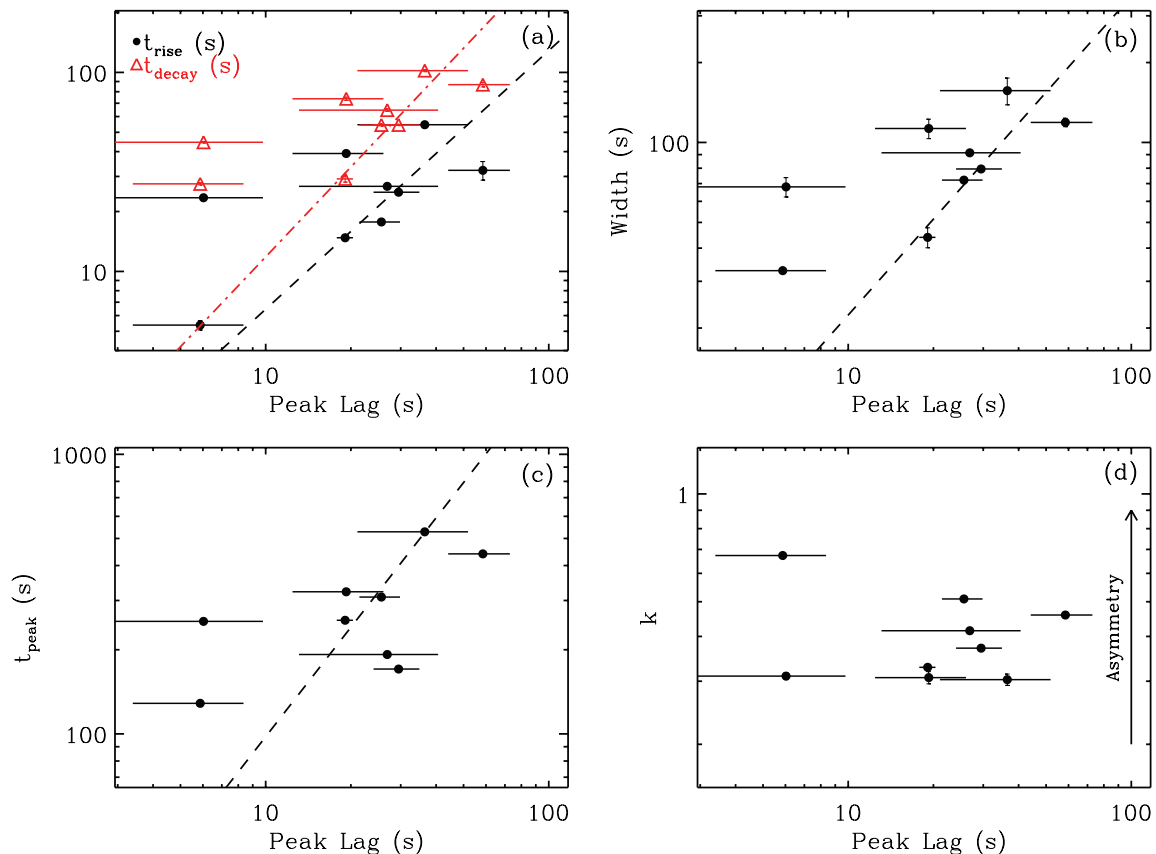
Figure 7. (a) Bright flare rise (red triangles) and decay times (black dots) versus peak lag. The red dot–dashed line and black dashed line indicate the best-fitting relations: $t_r = 10^{-0.49 \pm 0.28}(t_{\text{lag}})^{1.3 \pm 0.21}$; $t_d = 10^{-0.31 \pm 0.32}(t_{\text{lag}})^{1.5 \pm 0.24}$. (b) Width versus peak lag. The dashed line indicates the best-fitting relation: $w = 10^{0.15 \pm 0.27}(t_{\text{lag}})^{1.2 \pm 0.20}$. (c) Peak time versus peak lag. The dashed line indicates the best-fitting relation: $t_{\text{peak}} = 10^{0.69 \pm 0.28}(t_{\text{lag}})^{1.2 \pm 0.21}$. (d) Scatter plot of the asymmetry versus peak lag. No relation is apparent. The arrow points to the direction of growing asymmetry.

the emission, the lower is the evolution. The parameters describing the profile of softer flares undergo a substantial evolution from one energy band to the other (corresponding to higher $|\alpha|$ values), while the evolution of hard profiles is limited (lower $|\alpha|$ values). Fig. 10, panel b, confirms that the evolution of the rise time from one energy band to the other is more sensitive than the decay time to the average spectral hardness of the flare. Furthermore, it can be seen that t_r and t_d undergo a similar evolution with bandpass only in hard flares: the softer the flare, the higher is the difference between the t_r and t_d rate of evolution with energy, with the rise time always

evolving faster in energy. The presence of the trends depicted in the first and second panels from the top of Fig. 10 automatically translates into the results of the third one: since $w = t_r + t_d$, it is not surprising that the width is subject to a higher level of evolution in softer flares. No clear correlation is found between the rate of evolution of the asymmetry and the spectral hardness: however, it is worth noting that the asymmetry evolves in the four softer flares, while a limited level of evolution or no evolution is detected in the five hardest flares (shaded area of Fig. 10, bottom panel). This is a consequence of the results above.
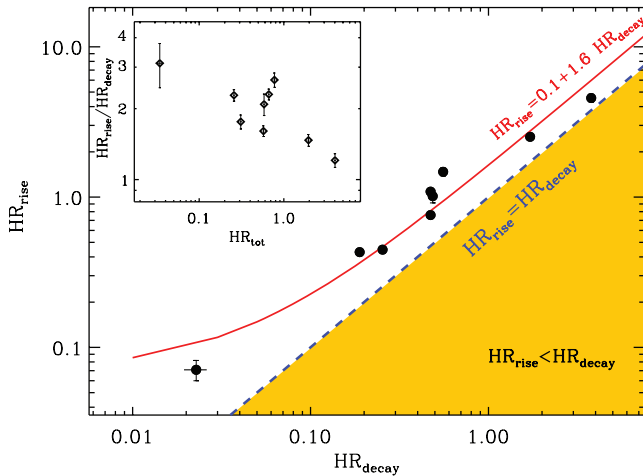
Figure 8. Hardness ratio of each flare during the rise time versus hardness ratio during the decay time: the flare spectrum is harder during the rise time. Red solid line: best-fitting linear relation: $\mathrm{HR_{rise}} = (0.07 \pm 0.01) + (1.6 \pm 0.1)\mathrm{HR_{decay}}$. Inset: rise time over decay time hardness ratio versus overall spectral hardness of the flares: a trend is apparent for harder flares to show more similar hardness ratios during the rise and decay portions of X-ray light curves.

At this point, a lag–hardness correlation is expected: Fig. 11 demonstrates that softer flares are characterized by larger time lags.

4.3 Spectral modelling

The flare emission is typical of the X-ray regime. The limited-energy window of the XRT (0.3–10 keV), as well as the complete ignorance of the distance of the emitting source coupled to a poor knowledge of the intrinsic neutral hydrogen column density absorbing the softest photons, can lead to the misidentification of intrinsically curved spectra in terms of absorbed power laws. We therefore select a subsample of flares with measured redshift and with contemporaneous detection by the BAT in the 15–150 keV: these requirements restrict the analysis to the two flares observed in GRB 060904B and GRB 060418.[5]

The very good statistics characterizing both signals gives us the possibility to perform a time-resolved spectral analysis. To follow the spectral evolution of the source, we time-sliced the BAT and XRT data of GRB 060418 and GRB 060904B into four and eight bins, covering the 129–320 and 122–170 s time intervals, respectively. The time intervals were defined so as to contain a minimum of ∼1000 photons in the XRT range and to possibly have enough signal in the BAT energy range to constrain the spectral parameters. The spectra were first fitted using an absorbed simple power-law (SPL) model within XSPEC: the model is absorbed by both a Galactic and an intrinsic absorption components. The Galactic component was frozen to the value specified by Kalberla et al. (2005) in the direction of the burst (which is taken to be the XRT refined position delivered by the *Swift*-XRT team); the intrinsic neutral hydrogen column density $N_{\mathrm{H},z}$ was left free to vary. When possible we took advantage of the simultaneous BAT and XRT coverage, performing a joint BAT–XRT spectral fit. The normalization for each instrument was always tied to the same value. The results are reported in

Tables A3 and A2. The SPL fit results are statistically unsatisfactory and are not able to account for the 15–150 keV data. Moreover, the best-fitting $N_{\mathrm{H},z}$ are inconsistent with the values obtained for both GRBs from late-time spectra, where no spectral evolution is detected and no spectral break is expected to lie in the XRT bandpass: for GRB 060904B and GRB 060418, from spectra extracted in the time intervals 1–500 ks and 200–1000 s, respectively, we obtained $N_{\mathrm{H},z} \sim (0.4 \pm 0.1) \times 10^{22}\,\mathrm{cm^{-2}}$ (90 per cent errors are provided). The SPL fits of Tables A3 and A2 instead indicate values $> 10^{22}\,\mathrm{cm^{-2}}$. These facts, together with the clear evolution of the best-fitting spectral photon index to softer values with time, suggest that the peak of the νF_ν spectrum is moving through the BAT+XRT bandpass. We tested this possibility performing time-resolved spectral fits to the empirical Band function (Band et al. 1993) using E_{p} as free parameter (NGRBEP model). The high and low power-law indices (α_{B} and β_{B}), which characterize the Band model, were used as free parameters: we froze α_{B} to the typical -1 (see e.g. Kaneko et al. 2006) value when poorly constrained. The uncertainties affecting each parameter were computed freezing α_{B} to the best-fitting value. The spectra of each flare were fitted simultaneously under the assumption of a constant $N_{\mathrm{H},z}$ during the flare emission. The results of the fitting procedure are listed in Tables A3 and A2 for GRB 060418 and GRB 060904B, respectively. The observed evolution of the peak energy with time is represented in Fig. 12: for both flares, E_{p} is found to evolve to lower values, with a decay that during the flare decay time can be represented by either a power law with index $\alpha \sim -7$ or an exponential with e-folding time $\tau = 29 \pm 5$s (GRB 060904B) and $\tau = 20 \pm 2$s (GRB 060418). The uncertainty of the intercalibration of the BAT and XRT has been investigated as possible source of the detected spectral evolution: for each time-slice, we multiplied the fit model by a constant factor which is frozen to 1 for the BAT data. For XRT, this factor is left free to vary between 0.9 and 1.1, conservatively allowing the XRT calibration to agree within 10 per cent with the BAT calibration. The best-fitting parameters found in this way are completely consistent with those listed in Tables A2 and A3. The intercalibration is therefore unlikely to be the main source of the observed evolution.

For each time interval we computed the isotropic equivalent luminosity L_{iso} in the rest-frame 1–10^4 keV energy band: these contributions have been de-absorbed for both the Galactic and intrinsic hydrogen column density (see Tables A2 and A3). The spectral peak energy is found to evolve in the L_{iso}–$E_{\mathrm{p,i}}$ plane following a power-law behaviour with best-fitting power-law index ∼1 (Fig. 13). In particular, for GRB 060418 (GRB 060904B) we have $E_{\mathrm{p,i}} \propto L_{\mathrm{iso}}^{1.0 \pm 0.2}$ and ($E_{\mathrm{p,i}} \propto L_{\mathrm{iso}}^{1.1 \pm 0.2}$)). For GRB 060904B we were able to extract a spectrum at the onset of the flare emission: the properties of this spectrum (green cross in Fig. 13, upper panel) are clear outliers with respect to the general trend defined by the other spectra. The same cannot be done for the GRB 060418 flare: in this case, a spectrum extracted at the onset is completely dominated by the contribution of the underlying continuum and nothing reliable can be said about the flare spectral properties in this time interval.

The average spectral properties of the two flares have been computed extracting a spectrum from $t_{\mathrm{peak}} - t_{\mathrm{r}}$ to $t_{\mathrm{peak}} + t_{\mathrm{d}}$ (shaded area of the insets of Fig. 12): in both cases the BAT detection rules out a SPL behaviour (χ^2/d.o.f. = 289.34/216, P-value = 6×10^{-4} and χ^2/d.o.f. = 466.45/304, P-value = 6×10^{-9} for GRB 060418 and GRB 060904B, respectively). The two spectra are instead well represented by a Band model with best-fitting observed peak energies $E_{\mathrm{p}} = 3.3^{+0.2}_{-0.3}$ keV (intrinsic value $E_{\mathrm{p,i}} = 8.2$ keV) for GRB 060418 and $E_{\mathrm{p}} = 3.7^{+0.2}_{-0.2}$ keV ($E_{\mathrm{p,i}} = 6.3$ keV) for GRB 060904B (90 per

---

[5] In spite of the measured redshift and BAT detection, GRB 060526 is excluded because of the partial overlap of the two structures.
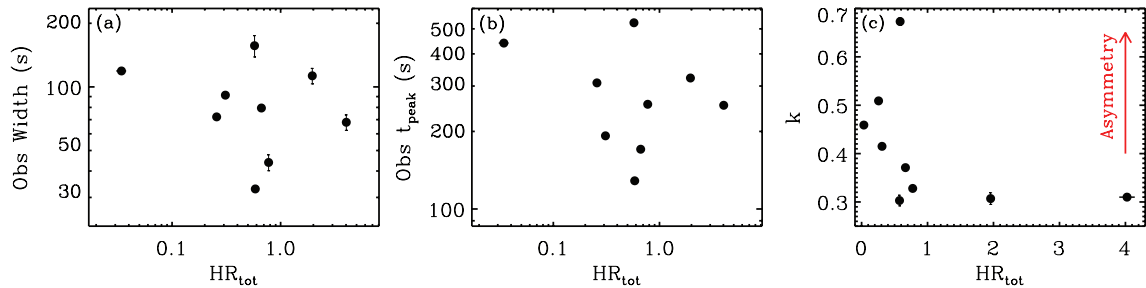
Figure 9. Best-fitting observed width (a), peak time (b) and asymmetry (c) as a function of the total hardness ratio. The red arrow in panel (c) points to the direction of higher asymmetry.

cent uncertainties are provided). The best-fitting results are reported in Table 2: note that the isotropic equivalent peak luminosity $L_{p,iso}$ is calculated starting from the time-*averaged* spectrum rescaled with the flare peak flux. In spite of not representing the real flare peak luminosity, this definition allows us to perform a direct comparison to the results obtained in the literature for the γ-ray prompt pulses (see e.g. Nava et al. 2008 and Yonetoku et al. 2004).

5 DISCUSSION

Through the analysis of nine bright X-ray flares we proved the existence of a set of correlations which link both the temporal and spectral flare parameters. The choice of this sample introduces an obvious caveat in our analysis, namely that we make the explicit assumption that the results we derive from the bright flares hold for all the flares. However, apart from the brightness, there is no evidence that our sample of bright flares is not representative of the entire population at the 80 per cent CL as obtained by a Kolmogorov–Smirnov (KS) test. We therefore conclude that our results are likely to be extended to the entire population of X-ray flares.

5.1 Temporal parameter evolution with energy

Flares have different temporal profiles in different energy bandpasses: in strict analogy to prompt emission pulses, flares are broader and peak later at lower energy. C10 found $w \propto E^{-0.5}$. Our sample of bright flares shows $w \propto E^{-0.3}$. For the prompt pulses the relation reads $w \propto E^{-0.4}$ (Fenimore et al. 1995, but see also Borgonovo et al. 2007; N05; Norris et al. 1996, and references therein). The width evolution results from the joint evolution of two time-scales: the rise and the decay times. The evolution with energy of t_r and t_d is well described by a power law, with power-law indices which are found to be very similar (see Table 1): however, the very good statistics of our sample allows us to conclude that the *rise* time is more sensitive to the energy bandpass than the decay time. This is evident from Fig. 6. Since the evolution of the temporal parameters with energy band is strictly linked to the spectral evolution during the flare emission, this would point to some spectral differences between the rise and decay portions of the light curve. In particular, the different relative position of the evolving E_p with respect to the fixed energy bands during the t_r and t_d is likely to play a major role: this can be in turn a footprint of two different physical mechanisms dominating the rise and the decay phases. The first consequence of this finding is that each energy channel is only nearly an exact time-stretched version of the others: flares can be treated as self-similar in energy only at the zeroth level of approximation. The second direct consequence is the presence of a slight trend pointing to more asymmetric flares at higher energy (Table 3, Fig. 5, panel d). Norris

et al. (1996), defining the asymmetry as t_r/t_d, found no evolution of this ratio with energy for GRB prompt pulses: however, the separate evolution $t_r(E)$ and $t_d(E)$ were not calculated.

While the soft energy flare profiles are clearly broader and peak later, it is unclear if the flares start simultaneously at all energies. The Pulse Start Conjecture was first proposed by Nemiroff (2000) and then tested by Hakkila & Nemiroff (2009): these authors studied a sample of 199 prompt Burst and Transient Source Experiment (BATSE) pulses in 75 different GRBs using an automatic pulse-fitting methodology. Each pulse is modelled by a N05 profile (the same profile used for flares). We caution that a strong coupling is built in the N05 profile between t_s and τ_1: the two parameters are clearly related since both fit the flares before the peak. This translates in a non-negligible probability of obtaining a good fit with perfect χ^2 but with non-physical t_s and τ_1: any slight but systematic variation $t_s(E)$ would be destroyed. The other two major problems are connected to the structure overlap and low statistics that affect part of the Hakkila & Nemiroff (2009) sample as discussed by the authors. In spite of these limitations the Pulse Start Conjecture was concluded to hold for prompt γ-ray pulses with an uncertainty of ~ 0.4 s. For the X-ray flares the situation is different: the selection of seven isolated flares with very good statistics led to the conclusion that a slight trend for flare profiles at *high* energy to start *later* is present. An example is shown in Fig. 2, panel (l). Table A1 reports the start time values for the entire sample of bright flares: the high-energy profile t_s is always larger than the low-energy t_s: in five cases out of seven the difference between the two values is significant at more than 3σ CL.

The flare emission preferentially builds up at lower energies at the beginning of the GRB flares.

Fig. 5 demonstrates that the rate of evolution of the temporal parameters with energy in a single flare can be markedly different from the average sample behaviour (see the values reported in Table 1 compared to those of Table 3). Notably, this is directly linked to the observed flare spectral properties as proven by Fig. 10: the harder the flare, the lower is the detected rate of evolution of the flare profile in different energy bands. Since *hard* flares also display a *limited* spectral evolution in the 0.3–10 keV energy range (insets of Fig. 8) (likely because their E_p lies outside the XRT energy band during the majority of the emission time), the result above implies a strict link between the spectral properties and the evolution of the temporal properties.

The same is true when the flare peak lag is considered: in the case of the prompt emission, the cross-correlation lag between energy bands was shown to anticorrelate with the BATSE spectral hardness ratio by Norris, Marani & Bonnel (2000); when *pulse* properties are considered instead of time-integrated *burst* properties, the result is that the pulse spectral hardness anticorrelates with
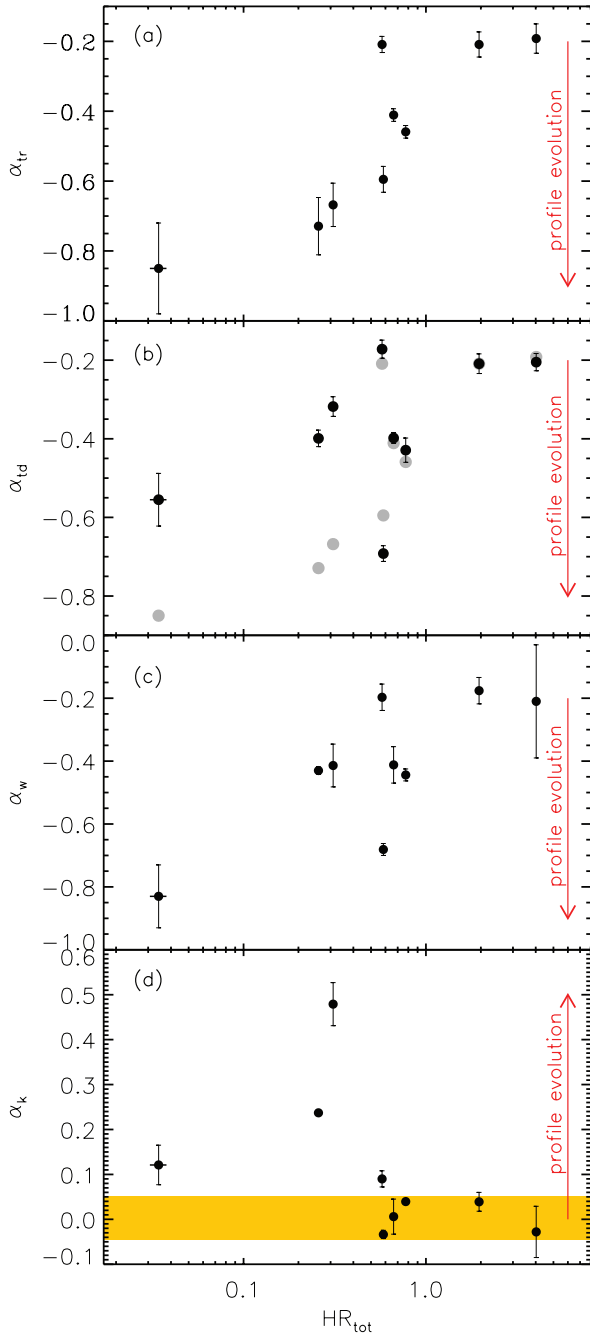
Figure 10. Best-fitting power-law index describing the evolution of the flare temporal profile parameters with observed energy (see Table 1) as a function of the spectral hardness of the flare. The evolution of each flare parameter with energy band has been fitted using the model: $y \propto E^\alpha$. (a) Rise time power-law indices. (b) Black dots: decay time power-law indices; grey dots: rise time power-law indices shown for direct comparison. (c) Width power-law indices. (d) Asymmetry power-law indices. The shaded area represents a region of low evolution. In each panel an arrow points to the direction of stronger spectral evolution of the parameter.

pulse lag and duration, and correlates with pulse intensity (Hakkila et al. 2008). Fig. 11 demonstrates that X-ray flares share the same property: a trend is evident for flares with larger HR_{tot} to have shorter peak lags. The lag–hardness correlation of this figure, together with Fig. 8, again implies a robust connection between the flares' temporal properties and their spectral evolution: a stronger
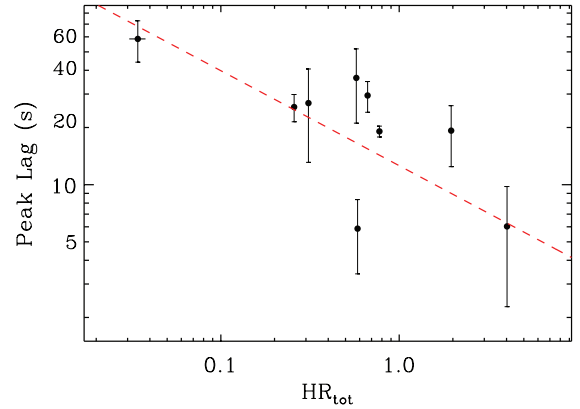
Figure 11. Observed pulse peak lag as a function of the spectral hardness of the flares. A power law with decaying index -0.5 is also shown for comparison (red dashed line).

spectral evolution directly translates into a higher lag. This means that the lag characterizing the flare profiles is the direct result of their spectral evolution. The same conclusion was reached by Kocevski & Liang (2003) for the prompt emission: these authors concluded that the fundamental origin of the observed lag is the evolution of the GRB prompt spectra to lower energies. Our results of Fig. 10 extend this finding to other flare temporal properties: the rate of evolution with energy of the rise time, decay time and width is inversely correlated to the spectral hardness and directly linked to the spectral evolution.

Finally we mention that only soft flares have been found to be highly asymmetric (Fig. 9, panel c). Similarly Norris et al. (1996) found that soft prompt pulses are on average more asymmetric.

5.2 The flare lag–luminosity relation

The flare peak lag is directly related to the flare duration (Table 3, Fig. 7) and since w has been found to vary inversely with the flare peak luminosity (C10, but see also the relation reported in Table 4), an inverse correlation between peak lag and luminosity is expected. Since only three flares in our sample have measured redshift, we selected the flares with the best statistics, measured redshift and well-defined peak times in both the hardest and softest XRT energy bands from the sample of C10. Fig. 14 confirms the expectation above, showing that the X-ray flares define a rather tight lag–luminosity relation:

$$\frac{L_{p,iso}^{0.3-10\,keV}}{(erg\,s^{-1})} = 10^{(50.82\pm0.20)} \left(\frac{t_{lag,x}}{s}\right)^{(-0.95\pm0.23)}, \qquad (9)$$

where $t_{lag,x}$ is the rest-frame peak lag calculated as the difference in time between the flare peak times in the 0.3–1 and 3–10 keV energy bands. The subscript x reminds that the time lag is calculated in the X-ray regime. We properly account for the sample variance following the method outlined by D'Agostini (2005). Errors are provided at 90 per cent CL. It is not possible to constrain the spectral peak energy and the spectral slopes of the majority of the flares of C10: for this reason we fitted the spectrum extracted around the peak time with an absorbed SPL within XSPEC and conservatively quote the isotropic peak luminosity as obtained in the observed 0.3–10 keV bandpass (black bullets in Fig. 14). In two cases, for GRB 060418 and GRB 060904B, the Band parameters were determined thanks to the BAT+XRT coverage (Table 2): this allows us to plot the 1–10 000 keV (rest-frame) isotropic peak luminosity. However, the best-fitting relation was derived using their 0.3–10 keV values for
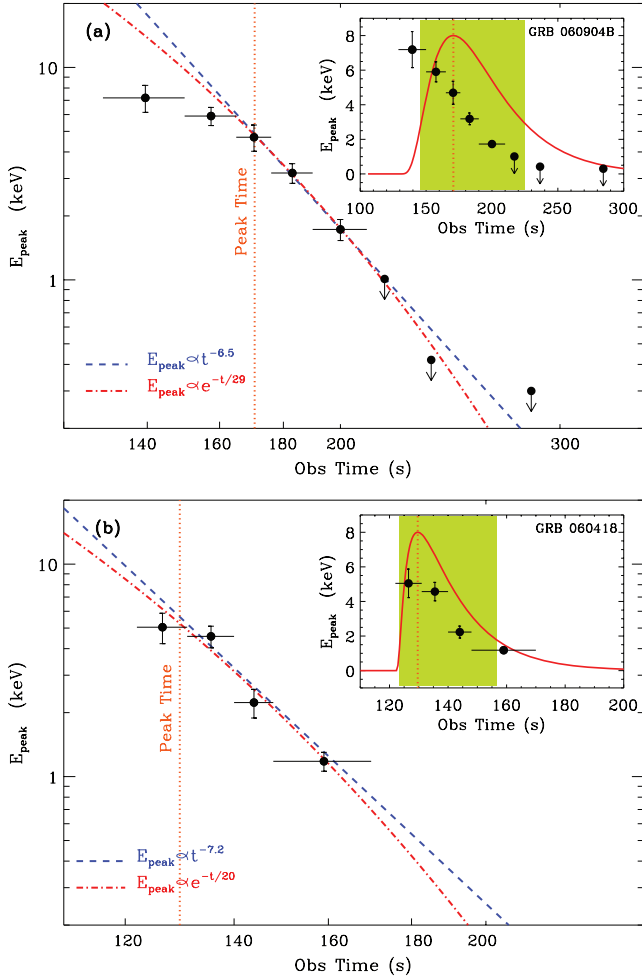
Figure 12. Temporal evolution of the observed peak energy of the νF_ν spectrum of the flare detected in GRB 060904B (panel a) and GRB 060418 (panel b). Blue dashed line: best-fitting power-law decay for the evolution of E_p during the decay time. The best-fitting power-law decay index is $\alpha_d = -7.2 \pm 0.7$ (GRB 060418) and $\alpha_d = -6.5 \pm 0.7$ (GRB 060904B). Red dot–dashed line: best-fitting exponential decay of E_p during the flare decay time. The zero time of the power law is assumed to be the BAT trigger time. The best-fitting e-folding time is found to be $\tau = 20 \pm 2$ and 29 ± 5 s for GRB 060418 and GRB 060904B, respectively. Insets: temporal evolution of E_p compared to the evolution of the 0.3–10 keV flare profile (red solid line). The flare flux is represented in arbitrary units. The shaded areas mark the interval of time of extraction of the average flare spectrum, from $t_{peak} - t_r$ to $t_{peak} + t_d$. In each panel, the orange dotted lines mark the flare peak time as derived from the best-fitting parameters.

homogeneity (the two red bullets in Fig. 14 consistently lie above the expectation). In the cases of the GRB 060418 and GRB 090904B flares, the isotropic peak luminosity in the 0.3–10 keV observed band underestimates the 1–10 000 keV rest-frame value of a factor of 2–3.

The lag–luminosity is one of the key relations which connects the GRB *prompt* temporal and spectral properties: discovered by Norris et al. (2000) as a time-integrated property of each particular burst, the relation was conclusively demonstrated to reflect *pulse* rather than *burst* properties by Hakkila et al. (2008). Fig. 14 shows a direct comparison between the flare and the prompt properties in the lag–luminosity diagram: this is of particular interest since long and short bursts are known to occupy different regions of the plane (see e.g. Gehrels et al. 2006). Flares in long GRBs are consistent
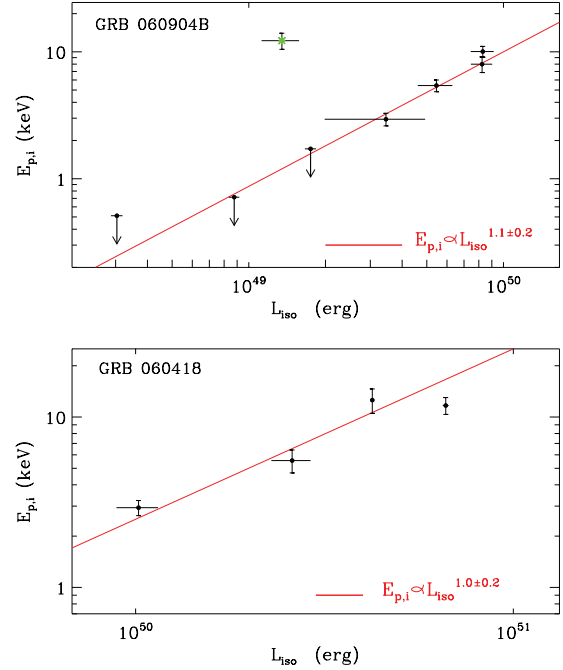
Figure 13. Time-resolved $E_{p,i}$–L_{iso} correlation for the flares detected in GRB 060904B (upper panel) and GRB 060418 (lower panel). Red solid lines: best-fitting power-law relations: $E_{p,i} \propto L_{iso}^{1.1\pm0.2}$; $E_{p,i} \propto L_{iso}^{1.0\pm0.2}$.

with the long-GRB lag–luminosity relation. However, we should consider that first, in Fig. 14 the lag of the prompt data is calculated using the cross-correlation function to the entire BAT light curve and consequently reflects a time-integrated property (see Ukwatta et al. 2010 for any detail). Secondly, for the prompt data the lag is defined as the time difference between light-curve structures in the 50–100 and 100–200 keV channels. For the flares we calculated the *peak* lag between X-ray energy bands. In both cases the lag has been computed between bandpasses around the event spectral peak energy. Thirdly, the prompt peak luminosity is calculated in the 1–10 000 keV rest-frame energy band, while for the flares the peak luminosity is calculated from the 0.3–10 keV (observed) bandpass (which is expected to be a factor of 2–3 below the 1–10 000 keV value).

With these caveats in mind, it is remarkable that the best-fitting slope of the flare lag–luminosity is consistent with the Ukwatta et al. (2010) results based on BAT data (see Table 5): $L_{p,iso} \propto t_{lag,\gamma}^{(-0.95\pm0.30)}$ (red dot–dashed line in Fig. 14). It is not surprising that this relation overestimates the flare luminosity which is computed in a narrower energy window by a factor of $\sim$5. Only a marginal consistency can be quoted with Hakkila et al. (2008) who reported an index $\sim$0.6. Our findings are instead fully consistent with the Norris et al. (2000) law (both in normalization and index), with a power-law index of 1.14 (blue dashed line in Fig. 14): these authors reported lags between BATSE energy bands 100–300 and 25–50 keV. The same is true if we consider the lag–luminosity power-law index by Schaefer (2007) who reported a value of 1.01. The prompt lag–luminosity relations are summarized in Table 5.

This result strongly suggests a common physical mechanism producing both the GRB prompt emission and the X-ray flare emission hundreds of seconds later. The lag–luminosity relation has been proven to be a fundamental law extending $\sim$5 decades in energy and $\sim$5 decades in time.

Table 2. Average spectral properties of the flares detected in GRB 060418 and GRB 060904B. The two spectra have been extracted in the time interval defined by $(t_{\text{peak}} - t_{\text{r}})$–$(t_{\text{peak}} + t_{\text{d}})$ which corresponds to the shaded area in the insets of Fig. 12. The fitting model is a photoelectrically absorbed Band function with E_{p} as free parameter (TBABS*ZTBABS*NGRBEP within XSPEC). The intrinsic hydrogen column density $N_{\text{H},z}$ is frozen to the value found from the joint fit of the time-resolved spectra (see Table A2 and A3). The Galactic absorption in the direction of the bursts has been accounted for following Kalberla et al. (2005). The isotropic equivalent energy E_{iso}, the isotropic equivalent luminosity L_{iso} and the isotropic equivalent peak luminosity $L_{\text{p,iso}}$ are computed in the 1–10^4 keV rest-frame energy range. $L_{\text{p,iso}}$ is calculated rescaling the *time-integrated* spectrum with the flare peak flux. Errors are provided at 90 per cent CL.

	GRB 060418	GRB 060904B
z	1.489	0.703
α_{B}	-0.9	-1.0
β_{B}	-2.30 ± 0.09	-2.47 ± 0.10
E_{p} (keV)	$3.3^{+0.2}_{-0.3}$	$3.7^{+0.2}_{-0.2}$
$N_{\text{H},z}$ (10^{22} cm^{-2})	0.59	0.52
E_{iso} (erg)	$(5.4 \pm 0.5) \times 10^{51}$	$(2.4 \pm 0.2) \times 10^{51}$
L_{iso} (erg s^{-1})	$(4.1 \pm 0.4) \times 10^{50}$	$(5.2 \pm 0.5) \times 10^{49}$
$L_{\text{p,iso}}$(erg s^{-1})	$(5.1 \pm 0.5) \times 10^{50}$	$(9.1 \pm 0.9) \times 10^{49}$
χ^2/d.o.f.	209.26/216	312.86/304
P-value	0.61	0.35

Table 3. First and second columns: summary of the best-fitting relations describing the parameter evolution with energy band. Third and fourth columns: rate of evolution $|\alpha|$ of the parameters with energy as a function of the spectral hardness: a $\downarrow$ ($\uparrow$) indicates inverse (direct) correlation. $\oslash$ means that no correlation has been found.

	E		HR
$w \propto$	$E^{-0.32 \pm 0.01}$	$|\alpha_{\text{w}}| \propto$	$\downarrow$
$t_{\text{r}} \propto$	$E^{-0.37 \pm 0.01}$	$|\alpha_{\text{tr}}| \propto$	$\downarrow$
$t_{\text{d}} \propto$	$E^{-0.29 \pm 0.01}$	$|\alpha_{\text{td}}| \propto$	$\downarrow$
$k \propto$	$E^{0.11 \pm 0.01}$	$|\alpha_k| \propto$	$\oslash$

5.3 Flare parameter correlations

At the zeroth level of approximation, the flare phenomenology summarized in Table 4 reduces to a set of four independent relations (namely equations 10, 11, 12 and 13). This consistently limits the available parameter space for any theoretical model aiming at explaining the flare phenomena.

The first fundamental relation expresses the concept that flare profiles tend to be self-similar both in energy and in time (C10),

$$t_{\text{r}} \sim 0.5\, t_{\text{d}}, \tag{10}$$

which implies $\tau_1 \sim 4\tau_2$: the N05 profile contains a degree of freedom (d.o.f.) which is not required by the data since the rising and decaying time-scales are not independent from one another; $t_{\text{r}} \sim w/3 \sim \tau_2$, $t_{\text{d}} \sim 2w/3 \sim 2\tau_2$ and $k \sim$ const. The pulse peak lag between two energy bands centred on E_1 and E_2 reads $t_{\text{lag}}(E_1, E_2) = t_{\text{s}}(E_2) + 2\tau_{2,E_2} - t_{\text{s}}(E_1) - 2\tau_{2,E_1} \sim 2(\tau_{2,E_2} - \tau_{2,E_1})$ since $t_{\text{s}}(E_2) \approx t_{\text{s}}(E_1)$ at the first level of approximation. τ_2 directly inherits the energy dependence of t_{r} and t_{d} (Table 3): $\tau_{2,E_2} = (E_2/E_1)^{-\alpha_\tau} \tau_{2,E_1}$ where $\alpha_\tau \sim 0.2$–0.7. This implies $t_{\text{lag}} \sim f(E_1, E_2)\tau_2$ where f is a factor of proportionality which

depends on E_1 and E_2. A lag–width correlation is consequently expected since $w \propto \tau_2$ (or alternatively a t_{lag}–t_{r} or t_{lag}–t_{d} relation).

The width–peak time linear correlation discussed by C10 introduces the concept of temporal *evolution*, which is the key to interpret the GRB X-ray flare phenomenology,

$$w \propto t_{\text{peak}}, \tag{11}$$

which automatically implies $t_{\text{r}} \propto t_{\text{peak}}$ and $t_{\text{d}} \propto t_{\text{peak}}$; considering the lag–width correlation of the previous paragraph, equation (11) translates into a lag–t_{peak} correlation.

The third fundamental relation links the flare peak lags to their peak luminosities, in strict analogy to the prompt emission:

$$L_{\text{p,iso}} \propto t_{\text{lag}}^{-0.95 \pm 0.23}. \tag{12}$$

Consequently, t_{r}, t_{d} and w will be linked to the flare peak luminosity. In turn, the peak luminosity is expected to evolve with time to lower values, as found: $L_{\text{p,iso}} \propto t_{\text{peak}}^{-2.7}$ although with a large scatter.

The fourth relation again describes the temporal *evolution* of the flare spectral properties:

$$\text{HR}(t) \propto t_{\text{peak}}^{-\alpha}. \tag{13}$$

Flares become softer and softer as time proceeds. As a result, inverse HR–t_{r}, HR–t_{d}, HR–w and HR–t_{lag} relations are automatically built. This completes the set of 28 correlations (or lack thereof) of Table 4. An important implication is that at the zeroth level of approximation, the physics underlying the flare emission determines that out of three time-scales describing the flare temporal profile (namely t_{r}, t_{d} and t_{peak}), only one d.o.f. survives.

As a second level approximation, one should consider that $t_{\text{s}} = t_{\text{s}}(E)$; $f = f(E_1, E_2, \alpha_\tau)$ which likely reflects the relative position of the spectral peak energy with respect to E_1 and E_2; $k = k(E)$ since the rise and decay time evolution with energy band slightly differs from one another (Fig. 6). Any theoretical model aiming at explaining the flare emission is asked to be consistent with these set of findings, together with the flare spectral properties discussed in the following paragraph. A critical revision of the existing models is in preparation.

5.4 Temporal evolution of a flare spectrum

5.4.1 $E_{\text{p}}(t)$

For the two flares with the highest statistics, we find that the flare spectrum is well described by an evolving Band function. In both cases the spectral peak energy evolves with time to lower values following an exponential decay which tracks the decay of the flare flux. After t_{peak} the N05 profile is progressively dominated by the $\exp(-t/\tau_2)$ factor, with the relative strength of the $\exp(-\tau_1/t)$ dropping quickly. Remarkably, in both flares, the temporal evolution of the spectral peak energy and the flux seem to share the same e-folding time: for the flare detected in GRB 060418 we have $\tau_2 = 22.2 \pm 0.4$s with $\tau_{E_{\text{p}}} = 20.0 \pm 2.0$ s; for the GRB 060904B flare we find $\tau_2 = 29.5 \pm 0.6$s in good agreement with $\tau_{E_{\text{p}}} = 29.0 \pm 4.7$ s.

The evolution of $E_{\text{p}}(t)$ to lower values during the pulse decay time is one of the signatures of the prompt emission as demonstrated by a number of studies (see e.g. Peng et al. 2009 and references therein for a recent study on single prompt pulses). The spectral peak energy of prompt pulses is found to evolve following a power law[6] $E_{\text{p}}(t) \sim t^{-\delta}$ with an evolutionary slope $\delta \sim 1$ (see Peng et al.

---

[6] The zero time is chosen to be the starting point of the rising segment.

Table 4. Summary of the relations which link the flare parameters. ↑ (↓) stands for the presence of a direct (inverse) proportionality. ⊘ means that no correlation has been found; $L_{p,iso}$ is in units of erg s^{-1}; temporal parameters are indicated in s. Errors are reported at 90 per cent CL for correlations involving the peak luminosity.

	$L_{p,iso}$	t_r	t_d	w	k	t_{lag}	HR	t_{peak}
$L_{p,iso}$	–	$10^{(50.9\pm0.4)}t_r^{(-1.58\pm0.48)}$	$10^{(51.5\pm0.5)}t_d^{(-1.55\pm0.49)}$	$10^{(51.8\pm3.9)}w^{(-1.7\pm0.3)}$	⊘	$10^{(52.82\pm0.20)}t_{lag}^{(-0.95\pm0.23)}$	↑	$10^{(54.8\pm4.0)}t_{peak}^{(-2.7\pm0.5)}$
t_r	–	–	$(2.1\pm0.3)+(0.45\pm0.03)t_d$	$\sim1/3$	⊘	$(1.3\pm0.3)+(0.68\pm0.09)t_{lag}$	→	$(4.0\pm0.3)+(0.06\pm0.01)t_{peak}$
t_d	–	–	–	$\sim2/3$	⊘	$(0.2\pm0.7)+(2.2\pm0.3)t_{lag}$	→	$(3.0\pm0.4)+(0.14\pm0.02)t_{peak}$
w	–	–	–	–	⊘	$(1.5\pm1.0)+(2.9\pm0.4)t_{lag}$	→	$(4.8\pm0.6)+(0.20\pm0.02)t_{peak}$
k	–	–	–	–	–	⊘	⊘	⊘
Lag	–	–	–	–	–	–	→	← →
HR	–	–	–	–	–	–	–	

2009 and references therein). The observed evolution of the flare $E_p(t)$ is instead much faster and inconsistent with the t^{-1} behaviour after rescaling the time to the beginning of the flare emission. Taking the GRB 060904B flare which starts at $t_s \sim 124$ s as an example, $E_p(171\,\mathrm{s}) \sim 4.7$ keV would imply $E_p(300\,\mathrm{s}) \sim 1.2$ keV if the t^{-1} behaviour is assumed: the observations instead constrain the $E_p(300\,\mathrm{s})$ to be well below the XRT bandpass, so that $E_p(300\,\mathrm{s}) < 0.3$ keV. While this could be the result of a wrong choice of the power-law zero time (the relevant time could be the ejection time instead of t_s, see Willingale et al. 2010 for details), further investigations are required to establish if the faster $E_p(t)$ evolution is a peculiar feature of the flare emission when compared to the prompt phenomenology.

5.4.2 Flares in the E_p–E_{iso} and E_p–$L_{p,iso}$ planes

The spectral analysis of Section 4.3 allows us to constrain the properties of two X-ray flares in the E_p–E_{iso} and E_p–$L_{p,iso}$ planes for the first time. Fig. 15 shows the result: when compared to the spectral properties of the prompt emission of 83 GRBs with measured redshift and well-constrained spectra (Nava et al. 2008; Ghirlanda, Nava & Ghisellini 2010), the two flares show higher E_{iso} and $L_{p,iso}$ than expected starting from their rest-frame spectral peak energy $E_{p,i}$. If the flares are part of the prompt emission, then they are not expected to share the time-integrated $E_{p,i}$–E_{iso} best-fitting normalization: however, Krimm et al. (2009) demonstrated that individual sequences of the same burst do follow the E_p–E_{iso} relation with a *higher* normalization (reflecting the fact that the total energy budget is distributed over the sequence, see Krimm et al. 2009, their fig. 14). The opposite is observed for the two flares. The E_p–$L_{p,iso}$ plane does not suffer from this effect, and time-integrated properties can be here directly compared to their time-resolved counterparts. In this plane the two flares are barely inside the 3σ best-fitting area: however, the peak luminosity is poorly sampled below 5×10^{50} erg s^{-1} and a deviation to lower spectral peak energies of the main sample cannot be excluded since the best-fitting relation is mainly established by high-luminosity data points. In this case the X-ray flares would belong to the same E_p–$L_{p,iso}$ as the prompt emission. Alternatively, and equally interesting, the flares do not follow the $E_{p,i}$–$L_{p,iso}$ relation of the prompt data. This possibility is suggested by the fact that the two flares are outliers of the $E_{p,i}$–$E_{p,iso}$ relation even when the effect of the time-resolved spectral analysis is taken into account. Whether this depends on the chosen integration energy band ($1–10^4$ keV) is currently under investigation.

For GRB 060418 the spectral properties during the prompt emission were measured (see Amati et al. 2008; Nava et al. 2008): $E_{p,i}^{\gamma\text{-ray}} = 572 \pm 143$ keV; $E_{iso}^{\gamma\text{-ray}} = (13 \pm 3) \times 10^{52}$ erg; $L_{p,iso}^{\gamma\text{-ray}} = 1.9 \times 10^{52}$ erg. The flare isotropic input comprises ~5 per cent of the isotropic γ-ray prompt energy while the flare isotropic peak luminosity is ~3 per cent the $L_{p,iso}^{\gamma\text{-ray}}$. The contribution of the flare emission is therefore well within the uncertainties estimated for the prompt parameters: this result helps to understand how much the unaccounted flare emission contributes to the scatter affecting the $E_{p,i}$–E_{iso} relation (Amati et al. 2008).

5.4.3 The flare $E_p(t)$–$L_{p,iso}(t)$ relation

The time-resolved analysis of the two flares with redshift and BAT detection reveals that the rest-frame spectral peak energy $E_{p,i}$ correlates with the isotropic luminosity L_{iso} within single flares. The same has been demonstrated to be true for the prompt pulses: the
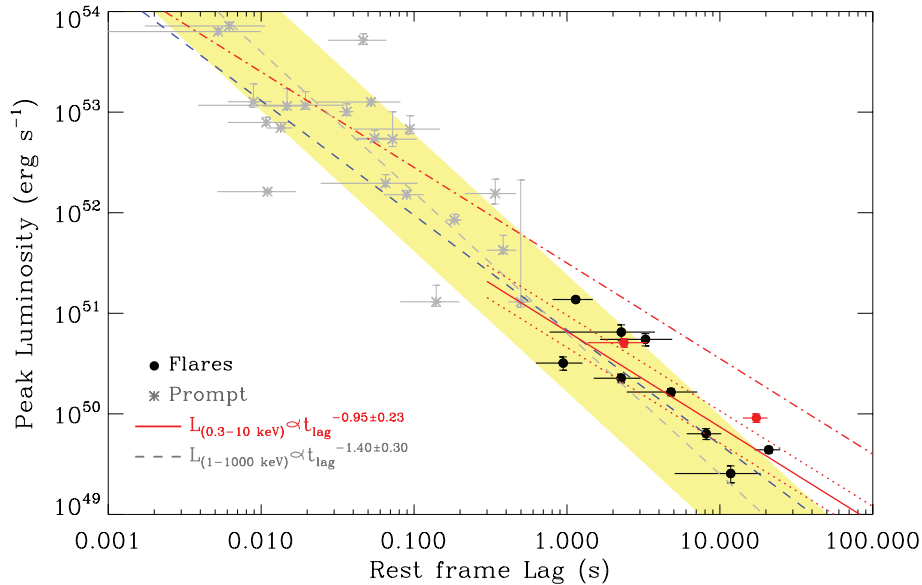
Figure 14. Flare peak lag–peak luminosity relation. Black filled circles: flares from C10. The isotropic peak luminosity has been computed in the observed 0.3–10 keV energy band. The two flares (in GRB 060418 and GRB 060904B) for which it was possible to estimate the Band parameters are marked with red bullets: in these cases the 1–10 000 keV peak luminosity is plotted (see Table 2). In both cases the flare peak lag is reported. Red solid line: flare best-fitting peak lag–peak luminosity relation; errors are provided at 90 per cent CL. Red dotted lines: best-fitting sample variance. Grey stars: prompt γ-ray data corresponding to the gold and silver samples of long GRBs from Ukwatta et al. (2010). The isotropic peak luminosity has been calculated in the 1–10 000 keV frame. The lag corresponds to the time difference between light-curve structures in the 50–100 and 100–200 keV channels. Grey dashed line: prompt best-fitting peak lag–peak luminosity relation from Ukwatta et al. (2010). The shaded area marks the 68 per cent region around this fit. Red dot–dashed line: best-fitting relation of the gold sample performed accounting for the sample variance. Blue dashed line: Norris, Marani & Bonnell (2000) lag–luminosity relation.

Table 5. Prompt γ-ray lag–luminosity relations.

	Sample	Reference
$\frac{L_{p,iso}}{(erg\,s^{-1})} = 10^{(51.5\pm0.4)} \left(\frac{t_{lag,\gamma}}{s}\right)^{(-0.95\pm0.30)}$	BAT	1[a]
$\frac{L_{p,iso}}{(erg\,s^{-1})} = 10^{(51.54\pm0.05)} \left(\frac{t_{lag,\gamma}}{s}\right)^{(-0.62\pm0.04)}$	BATSE	2[b]
$\frac{L_{p,iso}}{(erg\,s^{-1})} \sim 10^{53.1} \left(\frac{t_{lag,\gamma}}{0.01\,s}\right)^{(-1.14\pm0.10)}$	BATSE	3[c]

[a]Gold and silver sample from Ukwatta et al. (2010) fitted accounting for the sample variance, 90 per cent CL.
[b]Hakkila et al. (2008), on single pulses.
[c]Norris et al. (2000).

time-integrated correlations are the result of the existence of similar *time-resolved* correlations of the same parameters. Individual GRB prompt pulses are consistent with the $E_{p,i}$–L_{iso} as proved by Ghirlanda et al. (2010) and Ohno et al. (2009). This paper proves that two X-ray flares share this property and that flares in general are likely to be consistent with this behaviour. The best-fitting slopes of the two relations of Fig. 13 are however steeper than the ~ 0.5 slope found for the prompt emission (see e.g. Ghirlanda et al. 2010): whether this is something peculiar of the flare emission or not needs to be understood with a larger sample. At the moment we note that the best-fitting time-resolved $E_{p,i}$–L_{iso} slope within single prompt pulses has been found to be different from the 0.5 value in some cases: see e.g. GRB 090323 and GRB 090328 in Ghirlanda et al. (2010, their fig. 3), where the $E_{p,i}$–L_{iso} track seems to be steeper than 0.5.

Intriguingly, the spectrum extracted at the onset of the flare in GRB 060904B is a clear outlier, being characterized by an $E_{p,i}$ higher than expected: a similar result was found by Ohno et al. (2009) for the prompt emission. These authors performed a time-resolved spectral analysis of the GRB 061007 prompt emission and concluded that the *initial* rising phase of each pulse is an outlier of the $E_{p,i}$–L_{iso} relation, with $E_{p,i}$ around twice the value expected from the spectral correlation. However, no difference between the rise and decay portions of the prompt pulses has been reported by Ghirlanda et al. (2010) from the analysis of two *Fermi* GRBs.

The presence of these spectral correlations during the flare emission tightly links the X-ray flare emission to the prompt phase; as a by-product, these results strengthen the interpretation of the spectral energy correlations as manifestation of the physics of the GRBs (see Nava et al. 2008 and references therein for a detailed discussion of this topic).

5.5 Flares and light-curve morphology

The entire set of findings presented in this paper establishes a strong link between early X-ray flares and prompt pulses. Flares are consistent to be independent episodes of emission superimposed to the contemporary steep decay or afterglow components: while the first has been proven to be generated by the tail of the previous pulses (Kumar & Panaitescu 2000; see e.g. Willingale et al. 2010) and is therefore related to the physical mechanism which gives rise to the prompt emission, the latter is likely to be a completely independent component (e.g. Margutti et al. 2010).

X-ray afterglows with no breaks are likely to be dominated by the afterglow component from the beginning of the XRT observations (see Liang et al. 2009 for a dedicated study). We therefore expect the SPL X-ray afterglows to show a limited flaring component if flares really constitute an independent component (flares would be perhaps present but hidden by the contemporaneous afterglow emission). Fig. 16 confirms this expectation: the no-break class is clearly under-represented in the flare sample, while the vast majority
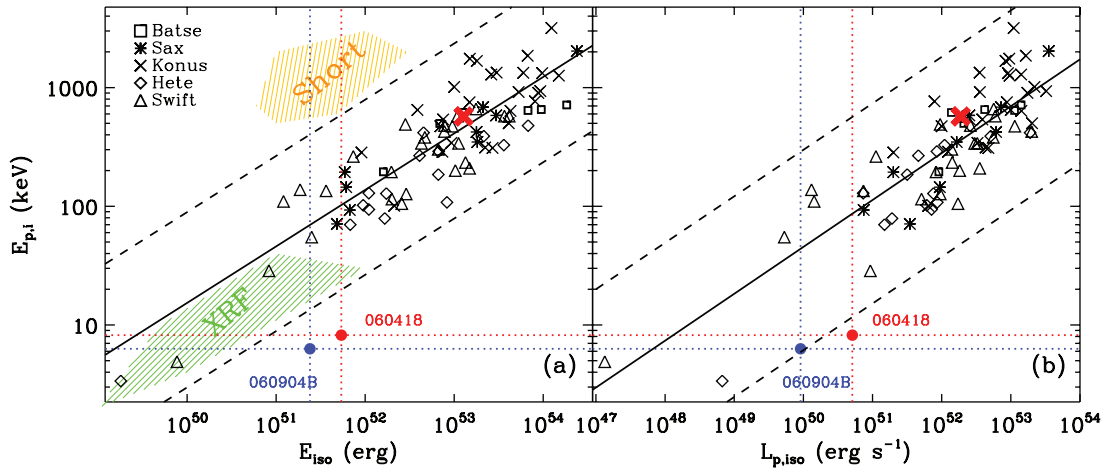
Figure 15. $E_{p,i}$–E_{iso} and $E_{p,i}$–$L_{p,iso}$ planes as obtained for the two X-ray flares detected in GRB 060904B and GRB 060418 (blue and red dots, respectively) superimposed to the data obtained from the sample of 83 GRBs with measured redshift and spectral parameters analysed in Nava et al. (2008). Black solid lines: best fit to the enlarged sample of 110 GRBs published in Ghirlanda et al. (2010), with best-fitting slopes $\delta = 0.476 \pm 0.025$ and 0.395 ± 0.024 for the left- and right-hand panels, respectively. The dashed lines represent the 3σ scatter. In both panels a red cross marks the *prompt* spectral properties of GRB 060418. The approximate position of short GRBs and XRFs in the $E_{p,i}$–E_{iso} plane is marked with shaded areas.
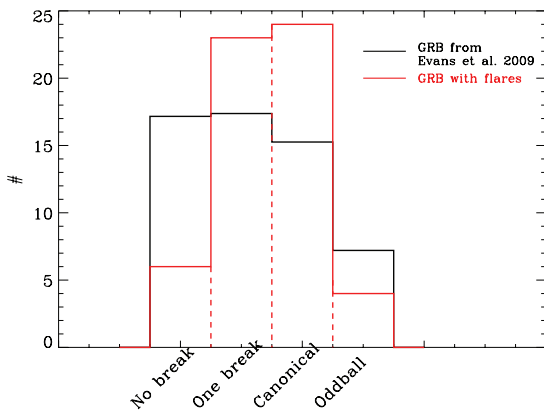
Figure 16. Red line: classification of the GRBs belonging to the flare sample of C10 according to their X-ray afterglow morphology (see Evans et al. 2009 for details). Black line: GRBs belonging to the Evans et al. (2009) sample detected in the same period of time. This distribution has been renormalized for the total number of GRBs of the flare sample.

Figure 17. Flare paradigm. Dashed curves: high-energy profile. Solid line: low-energy profile. High-energy profiles rise faster, decay faster and peak before the low-energy emission. As time proceeds, flares become wider, with higher peak lag, lower peak luminosities and softer emission. However, at the zeroth level of approximation the self-similarity is preserved both in energy and in time (with $t_r/t_d \sim 0.5$). We stress that this is an *average* behaviour. The thick solid arrow underlines the dependence of the flare properties on *time*, in strong opposition to prompt pulses.

of the detected early-time flares reside in one-break or canonical X-ray afterglows. The probability that the two samples are drawn from the same population is evaluated to be as low as 0.9 per cent using a KS test. If this is due to the brightness of the afterglow emission, then the conclusion is that flares have an independent origin: in the standard scenario this means that flares are not produced by the external shock. Another equally interesting possibility is that flaring emission is quenched (instead of being hidden) in SPL-afterglow GRBs. Distinguishing between these two possibilities is beyond the scope of this paper and will be the subject of a forthcoming investigation.

6 SUMMARY AND CONCLUSIONS

The GRB X-ray flare phenomenology shows a list of properties strictly analogous to the γ-ray prompt emission (see Hakkila et al. 2008 for a recent study on individual prompt pulses). However, it

differs in one crucial aspect: flares *evolve* with *time*.[7] Flares evolve with time to lower peak intensities, larger widths, larger lags and softer emission. Fig. 17 illustrates the flare paradigm. As the prompt emission pulses, flares have correlated properties: short-lag flares have shorter duration, are more luminous and harder than long-lag flares. In particular the following properties add to the lists of Section 1.

---

[7] We parenthetically note that this difference could be due to the fact that the relevant time for a peak (prompt pulse or flare) is the time since the shell ejection in a standard internal shock scenario, and not the time since trigger. While these two time-scales are completely unrelated for the prompt pulses, they are more closely related for flares (since the time is large the difference between the two becomes negligible). See Willingale et al. (2010) and Willingale et al. (in preparation) for further details.

(i) Flares define a lag–luminosity relation: $L_{\mathrm{p,iso}}^{0.3-10\,\mathrm{keV}} \propto t_{\mathrm{lag}}^{-0.95\pm0.23}$. The best-fitting slope is remarkably consistent with the prompt findings (see Ukwatta et al. 2010 and references therein for a recent study).

(ii) The lag is found to correlate with the flare width while it is inversely correlated to the flare spectral hardness.

(iii) The flare temporal profiles in different bandpasses are only a nearly exact time-stretched version of one another: the rise and decay times evolve following slightly different power laws in energy: $t_r \propto E^{-\alpha_{\mathrm{tr}}}$, $t_d \propto E^{-\alpha_{\mathrm{td}}}$ with $\alpha_{\mathrm{tr}} > \alpha_{\mathrm{td}}$. The result is that flares are on average more asymmetric at high energy.

(iv) The rate of evolution of a flare profile in different bandpasses anticorrelates with its spectral hardness: the harder the flare the lower is the rate of evolution from one energy band to the other.

(v) The flare spectral peak energy $E_{\mathrm{p}}(t)$ evolves to lower values following an exponential decay which tracks the decay of the flare flux. The detected evolution is faster and inconsistent with the $\sim t^{-1}$ behaviour even when the zero time is reset to the beginning of the flare emission.

(vi) The two flares with best statistics show higher than expected E_{iso} and $L_{\mathrm{p,iso}}$ values when compared to the $E_{\mathrm{p,i}}$–E_{iso} and $E_{\mathrm{p,i}}$–L_{iso} prompt correlations.

(vii) The rest-frame spectral peak energy $E_{\mathrm{p,i}}$ correlates with the isotropic luminosity L_{iso} within single flares, giving rise to a time-resolved $E_{\mathrm{p,i}}$–L_{iso} correlation.

(viii) The flare emission preferentially builds up at lower energies: flares do not seem to be consistent with the Pulse Start Conjecture.

(ix) Among the different types of X-ray afterglow light curves, the SPL afterglows are under-represented in the flare sample. Flares are preferentially detected superimposed to one-break or canonical light curves.

The strict analogy between the prompt pulse and flare phenomenology strongly suggests a common origin of the two phenomena.

ACKNOWLEDGMENTS

REFERENCES

Amati L., Guidorzi C., Frontera F., Della Valle M., Finelli F., Landi R., Montanari E., 2008, MNRAS, 391, 577

Band D. et al., 1993, ApJ, 413, 281

Barthelmy S. D. et al., 2005a, Space Sci. Rev., 120, 143

Barthelmy S. D. et al., 2005b, Nat, 438, 994

Borgonovo L., Frontera F., Guidorzi C., Montanari E., Vetere L., Soffitta P., 2007, A&A, 465, 765

Burrows D. N. et al., 2005a, Space Sci. Rev., 120, 165

Burrows D. N., Romano P., Falcone A., 2005b, Sci, 309, 1833

Chincarini G. et al., 2007, ApJ, 671, 1903 (C07)

Chincarini G. et al., 2010, MNRAS, in press (doi:10.1111/j.1365-2966.2010.17037.x) (this issue; C10)

Curran P. A., Starling R. L. C., O Brien P. T., Godet O., van der Horst A. J., Wijers R. A. M. J., 2008, A&A, 487, 533

Curran P. A., Page K. L., Cummings J. R., Barthelmy S. D., Marshall F. E., 2009, GCN Rep., 223.1

D'Agostini G., 2005, preprint (physics/0511182)

Evans P. A. et al., 2009, MNRAS, 397, 1177

Falcone A. D. et al., 2006, ApJ, 641, 1010

Falcone A. D. et al., 2007, ApJ, 671, 1921 (F07)

Fenimore E. E., Zand J. J. M., Norris J. P., Bonnell J. T., Nemiroff R. J., 1995, ApJ, 448, L101

Ford L. A. et al., 1995, ApJ, 439, 307

Gehrels N. et al., 2004, ApJ, 611, 1005

Gehrels N. et al., 2006, Nat, 444, 1044

Ghirlanda G., Nava L., Ghisellini G., 2010, A&A, 511, 43

Goad M. R. et al., 2007, A&A, 468, 103

Godet O. et al., 2007, A&A, 471, 385

Greiner J. et al., 2009, ApJ, 693, 1912

Hakkila J., Nemiroff R. J., 2009, ApJ, 705, 372

Hakkila J., Giblin T. W., Norris J. P., Fragile P. C., Bonnell J. T., 2008, ApJ, 677, L81

Kalberla P. M. W. et al., 2005, A&A, 440, 775

Kaneko Y., Preece R. D., Briggs M. S., Paciesas W. S., Meegan C. A., Band D., 2006, ApJS, 166, 298

Klebesadel R. W., Strong I. B., Olson R. A., 1973, ApJ, 182, L85

Klotz A. et al., 2008, A&A, 483, 847

Kocevski D., Liang E., 2003, ApJ, 594, 385

Kouveliotou C. et al., 1993, ApJ, 413, L101

Krimm H. A. et al., 2007, ApJ, 665, 554

Krimm H. A. et al., 2009, ApJ, 704, 1405

Kumar P., Panaitescu A., 2000, ApJ, 541, L51

Lazzati D., Perna R., Begelman M. C., 2008, MNRAS, 388, L15

Liang E. W., Lu H. J., Hou S. J., Zhang B. B., Zhang B., 2009, ApJ, 707, 328

Margutti R. et al., 2008, A&A, 480, 677

Margutti R. et al., 2010, MNRAS, 402, 46

Moretti A. et al., 2005, in Siegmund O. H. W., ed., Proc. SPIE Vol. 5898, UV, X-ray, and Gamma-ray Space Instrumentation for Astronomy XIV. SPIE, Bellingham, p. 360

Moretti A. et al., 2008, A&A, 478, 409

Nava L., Ghirlanda G., Ghisellini G., Firmani C., 2008, MNRAS, 391, 639

Nemiroff R. J., 2000, ApJ, 544, 805

Norris J. P. et al., 1996, ApJ, 459, 393

Norris J. P., Marani G. F., Bonnell J. T., 2000, ApJ, 534, 248

Norris J. P. et al., 2005, ApJ, 627, 324 (N05)

Ohno M., Ioka K., Yamaoka K., Tashiro M., Fukazawa Y., Nakagawa Y. E., 2009, PASJ, 61, 201

Peng Z. Y., Ma L., Zhao X. H., Yin Y., Fang L. M., Bao Y. Y., 2009, ApJ, 698, 417

Ramire-Ruiz E., Fenimore E. E., 2000, ApJ, 539, 712

Romano P. et al., 2006a, A&A, 456, 917

Romano P. et al., 2006b, A&A, 450, 59

Salvaterra R. et al., 2009, Nat, 461, 1258

Schaefer E. B., 2007, ApJ, 660, 16

Tanvir N. R. et al., 2009, Nat, 461, 1254

Ukwatta T. N. et al., 2010, ApJ, 711, 1073

Vaughan S. et al., 2006, ApJ, 638, 920

Willingale R., Genet F., Granot J., O'Brien P. T., 2010, MNRAS, 403, 1296

Yonetoku D., Murakami T., Nakamura T., Yamazaki R., Inoue A. K., Ioka K., 2004, ApJ, 609, 935

APPENDIX A: TABLES

Table A1. Flare best-fitting parameters according to equation (1) and derived quantities (equations 2, 3, 4 and 5). The reported uncertainties are calculated accounting for the entire covariance matrix for each fit. From left- to right-hand side: GRB name, energy band of investigation, redshift, normalization, start time, first shape parameter, second shape parameter, peak time, width, asymmetry, rise time, decay time, chi squared and d.o.f. In each column, a −1 indicates the absence of the value in the literature (for the redshift) or the impossibility to constrain the value from the fit. A negative error indicates that the parameter was first left free to vary in the fit and then frozen to the reported value to constrain the errors associated to the other fit parameters.

GRB	Band	z	Norm (counts s^{-1})	t_s (s)	τ_1 (s)	τ_2 (s)	t_{peak} (s)	w (s)	k	t_r (s)	t_d (s)	χ^2	d.o.f.
050822	tot[a]	−1.0	45.5 ± 1.3	389.2 ± 7.5	48.0 ± 18.0	54.6 ± 3.1	440.4 ± 8.3	119.0 ± 4.4	0.459 ± 0.007	32.2 ± 3.4	86.8 ± 2.3	283.6	267
	1[b]	−1.0	22.3 ± 0.8	374.0 ± 13.0	123.0 ± 47.0	53.6 ± 4.6	455.2 ± 12.6	142.4 ± 13.2	0.376 ± 0.013	44.4 ± 3.8	98.0 ± 3.1	324.2	290
	2[c]	−1.0	20.2 ± 1.0	371.0 ± 16.0	85.0 ± 56.0	38.3 ± 4.1	428.1 ± 16.2	101.0 ± 18.0	0.379 ± 0.014	31.4 ± 5.3	69.7 ± 3.2	259.4	181
	3[d]	−1.0	5.0 ± −1.0	375.0 ± −1.0	21.0 ± 19.0	22.4 ± 6.8	396.7 ± 6.9	49.4 ± 4.3	0.453 ± 0.021	13.5 ± 2.1	35.9 ± 5.2	12.7	18
	4[e]	−1.0	−1.0	−1.0	−1.0	−1.0	−1.0	−1.0	−1.0	−1.0	−1.0	−1.0	−1.0
060418	tot	1.489	379.1 ± 7.9	121.9 ± 0.2	2.0 ± 0.3	22.2 ± 0.4	128.6 ± 0.4	32.9 ± 0.4	0.673 ± 0.008	5.4 ± 0.3	27.5 ± 0.3	1665.1	975
	1	1.489	52.6 ± 1.6	111.8 ± 1.4	15.9 ± 4.1	31.4 ± 1.2	134.1 ± 2.5	61.6 ± 1.4	0.510 ± 0.008	15.1 ± 1.1	46.5 ± 1.1	644.4	497
	2	1.489	166.7 ± 4.1	118.6 ± 0.4	8.3 ± 1.3	19.4 ± 0.4	131.3 ± 0.9	36.9 ± 0.6	0.526 ± 0.005	8.8 ± 0.4	28.2 ± 0.5	1328.2	876
	1	1.489	83.8 ± 3.1	119.9 ± 0.6	8.0 ± 2.1	10.9 ± 0.6	129.3 ± 1.0	22.9 ± 0.6	0.475 ± 0.005	6.0 ± 0.4	16.9 ± 0.5	408.5	296
	4	1.489	121.8 ± 4.9	121.1 ± 0.3	5.5 ± 0.6	9.5 ± 0.4	128.3 ± 0.3	19.0 ± 0.6	0.498 ± 0.005	4.8 ± 0.1	14.3 ± 0.5	491.0	308
060526f[f]	tot	3.221	282.9 ± 5.6	225.0 ± 1.9	62.0 ± 15.0	14.4 ± 1.3	254.9 ± 2.3	43.9 ± 3.8	0.328 ± 0.006	14.8 ± 0.4	29.2 ± 1.1	1024.5	948
	1	3.221	49.7 ± 1.5	220.0 ± 0.0	95.0 ± 9.3	24.5 ± 3.2	268.2 ± 1.2	73.0 ± 3.8	0.336 ± 0.006	24.2 ± 1.4	48.7 ± 4.6	823.0	642
	2	3.221	143.8 ± 3.4	228.0 ± 0.0	53.5 ± 2.3	15.1 ± 0.7	256.3 ± 0.3	43.9 ± 0.8	0.342 ± 0.002	14.4 ± 0.3	29.5 ± 0.9	1306.2	850
	3	3.221	64.2 ± 2.2	230.0 ± 0.0	35.6 ± 2.3	12.7 ± 0.6	253.3 ± 0.4	35.3 ± 0.7	0.361 ± 0.002	11.3 ± 0.2	24.0 ± 0.8	495.3	294
	4	3.221	146.0 ± 3.9	232.0 ± 0.0	28.9 ± 1.2	10.2 ± 0.3	249.2 ± 0.2	28.3 ± 0.4	0.360 ± 0.001	9.1 ± 0.1	19.3 ± 0.4	619.8	365
060526s[g]	tot	3.221	148.9 ± 4.0	282.3 ± 1.0	18.8 ± 2.4	36.7 ± 0.8	308.6 ± 1.5	72.1 ± 0.8	0.509 ± 0.002	17.7 ± 0.7	54.4 ± 0.6	1024.5	948
	1	3.221	44.1 ± 3.1	284.6 ± 3.0	33.3 ± 8.0	41.5 ± 1.8	321.8 ± 3.8	88.8 ± 1.9	0.467 ± 0.005	23.7 ± 1.6	65.2 ± 1.3	823.0	642
	2	3.221	84.6 ± 2.6	285.6 ± 1.3	16.1 ± 3.1	30.8 ± 0.9	307.9 ± 1.9	60.7 ± 0.9	0.507 ± 0.004	15.0 ± 0.9	45.7 ± 0.7	1306.2	850
	3	3.221	27.3 ± 1.4	288.9 ± 1.0	4.3 ± 1.7	28.2 ± 1.5	299.9 ± 2.0	45.1 ± 1.6	0.625 ± 0.015	8.5 ± 1.2	36.7 ± 1.3	495.3	294
	4	3.221	26.3 ± 1.5	288.4 ± 0.9	2.2 ± 1.0	27.2 ± 0.0	296.1 ± 1.8	39.8 ± 0.4	0.684 ± 0.001	6.3 ± 1.2	33.5 ± 1.2	619.8	365
060904B	tot	0.703	392.0 ± 5.2	124.4 ± 0.9	72.4 ± 5.4	29.5 ± 0.6	170.6 ± 1.3	79.5 ± 1.5	0.371 ± 0.004	25.0 ± 0.4	54.5 ± 0.4	872.3	771
	1	0.703	47.6 ± 1.1	112.0 ± 4.6	176.0 ± 34.0	36.5 ± 2.6	192.1 ± 5.1	114.2 ± 9.4	0.320 ± 0.029	38.8 ± 1.0	75.3 ± 2.3	445.3	405
	2	0.703	169.9 ± 2.6	114.0 ± 1.9	160.0 ± 17.0	25.0 ± 0.8	177.2 ± 2.5	83.3 ± 5.7	0.300 ± 0.014	29.2 ± 0.5	54.1 ± 0.6	907.1	875
	3	0.703	75.7 ± 1.7	123.1 ± 2.3	92.0 ± 16.0	21.4 ± 1.0	167.5 ± 2.9	65.2 ± 5.0	0.328 ± 0.013	21.9 ± 0.7	43.3 ± 0.7	408.0	372
	4	0.703	114.1 ± 2.4	123.1 ± 1.5	92.0 ± 12.0	17.0 ± 0.6	162.7 ± 1.9	54.6 ± 3.9	0.312 ± 0.009	18.8 ± 0.4	35.8 ± 0.5	527.4	437
060929	tot	−1.0	68.6 ± 0.9	410.7 ± 5.9	290.0 ± 49.0	47.5 ± 1.6	528.1 ± 8.1	156.7 ± 18.1	0.303 ± 0.011	54.6 ± 1.9	102.1 ± 1.2	652.5	517
	1	−1.0	14.5 ± 0.4	410.0 ± 0.0	366.0 ± 21.0	53.4 ± 2.4	549.8 ± 1.8	180.9 ± 4.7	0.295 ± 0.005	63.7 ± 1.0	117.1 ± 3.3	278.6	226
	2	−1.0	29.3 ± 0.6	410.0 ± 0.0	306.0 ± 14.0	46.7 ± 1.3	529.5 ± 1.4	156.6 ± 3.4	0.298 ± 0.003	54.9 ± 0.5	101.6 ± 1.7	470.6	382
	3	−1.0	11.9 ± 0.4	432.0 ± 13.0	157.0 ± 81.0	46.2 ± 3.7	517.2 ± 19.0	133.7 ± 28.9	0.346 ± 0.016	43.7 ± 5.6	89.9 ± 3.3	143.5	135
	4	−1.0	17.4 ± 0.5	436.0 ± 10.0	130.0 ± 58.0	46.0 ± 2.8	533.3 ± 15.3	127.8 ± 20.8	0.360 ± 0.012	40.9 ± 4.8	86.9 ± 3.1	263.2	187
070520B	tot	−1.0	78.7 ± 1.4	146.6 ± 1.8	55.0 ± 7.6	37.9 ± 1.2	192.3 ± 2.5	91.4 ± 1.8	0.415 ± 0.006	26.8 ± 0.9	64.7 ± 0.9	480.2	431
	1	−1.0	21.4 ± 0.6	92.0 ± 11.0	420.0 ± 130.0	31.9 ± 2.9	207.8 ± 13.1	125.6 ± 50.2	0.254 ± 0.137	46.9 ± 2.0	78.8 ± 2.0	265.6	262
	2	−1.0	39.1 ± 1.0	134.1 ± 3.2	104.0 ± 19.0	32.0 ± 1.6	191.8 ± 4.1	91.7 ± 5.6	0.349 ± 0.014	29.8 ± 1.1	61.8 ± 1.2	460.4	365
	3	−1.0	12.0 ± 0.6	152.7 ± 4.0	31.0 ± 16.0	30.7 ± 2.9	183.6 ± 6.8	68.8 ± 3.7	0.446 ± 0.014	19.0 ± 2.6	49.7 ± 2.0	137.2	93
	4	−1.0	13.4 ± 0.8	164.3 ± 2.1	8.1 ± 4.5	33.9 ± 2.7	180.9 ± 4.1	58.3 ± 2.7	0.582 ± 0.019	12.2 ± 2.3	46.1 ± 2.1	131.5	102
070704	tot	−1.0	85.4 ± 1.3	238.9 ± 3.5	201.0 ± 30.0	34.6 ± 1.7	322.3 ± 4.3	112.9 ± 9.5	0.307 ± 0.012	39.1 ± 0.8	73.7 ± 1.3	537.2	498
	1	−1.0	1.8 ± 0.2	220.0 ± 0.0	300.0 ± 0.0	41.8 ± 3.5	332.0 ± 4.6	143.1 ± 9.1	0.292 ± 0.010	50.6 ± 2.8	92.4 ± 6.3	8.9	20
	2	−1.0	25.4 ± 0.7	256.9 ± 3.7	84.0 ± 18.0	54.0 ± 2.5	324.2 ± 5.9	132.1 ± 4.6	0.409 ± 0.007	39.1 ± 2.0	93.1 ± 1.8	370.7	316
	3	−1.0	20.7 ± 0.6	250.7 ± 4.3	104.0 ± 24.0	44.7 ± 2.5	318.9 ± 6.2	119.1 ± 6.6	0.375 ± 0.009	37.2 ± 1.9	81.9 ± 1.8	308.3	240
	4	−1.0	38.6 ± 0.9	249.7 ± 3.5	104.0 ± 22.0	38.2 ± 2.3	312.7 ± 5.0	105.3 ± 5.7	0.363 ± 0.009	33.6 ± 1.3	71.8 ± 1.7	410.4	362
090621A	tot	−1.0	325.8 ± 4.9	203.1 ± 2.3	116.0 ± 16.0	21.1 ± 0.6	252.6 ± 2.7	68.0 ± 5.7	0.310 ± 0.007	23.5 ± 0.7	44.6 ± 0.4	1006.6	636
	1	−1.0	−1.0	−1.0	−1.0	−1.0	−1.0	−1.0	−1.0	−1.0	−1.0	−1.0	−1.0
	2	−1.0	53.2 ± 1.4	197.5 ± 4.5	156.0 ± 30.0	24.1 ± 1.4	258.8 ± 4.2	80.6 ± 9.9	0.299 ± 0.014	28.2 ± 0.8	52.3 ± 1.2	380.8	346
	3	−1.0	69.7 ± 1.7	199.1 ± 4.8	150.0 ± 37.0	20.5 ± 1.2	254.6 ± 5.4	70.5 ± 13.8	0.291 ± 0.017	25.0 ± 1.1	45.5 ± 0.8	452.0	375
	4	−1.0	194.1 ± 3.6	199.3 ± 3.2	144.0 ± 26.0	18.5 ± 0.7	251.0 ± 3.8	64.6 ± 9.8	0.290 ± 0.012	23.0 ± 0.8	41.6 ± 0.5	1000.3	726

[a]0.3–10 keV.
[b]0.3–1 keV.
[c]1–2 keV.
[d]2–3 keV.
[e]3–10 keV.
[f]First flare detected by the XRT.
[g]Second flare detected by the XRT.

Table A2. Best-fitting parameters derived from the spectral modelling of the XRT and BAT data of GRB 060904B. A photoelectrically absorbed models (TBABS*ZTBABS within XSPEC). Two different spectral models have been used: a SPL and a Band function with the peak of the νF_ν spectrum as free parameter. From left- to right-hand side: name of the interval of the extraction of the spectrum: XRT+BAT stands for a joint BAT–XRT data fitting, start and stop time of extraction of each spectrum, model used, intrinsic neutral hydrogen column density, best-fitting low- and high-energy photon indices for a Band function or best-fitting photon index Γ for a SPL model, spectral peak energy, isotropic luminosity, statistical information about the fit. The * symbol indicates an apparent trend in the residuals of the fit. A joint fit of all the spectra gives $N_{H,z} = 0.5 \pm 0.1$, χ^2/d.o.f. $= 579.76/567$, P-value $= 35$ per cent. The Galactic absorption has been frozen to 1.13×10^{21} cm^{-2} (Kalberla et al. 2005). Errors are provided at 90 per cent CL.

	Interval	t_i (s)	t_f (s)	Model	$N_{H,z}$ (10^{22} cm^{-2})	α_B	$\beta_B(\Gamma)$	E_{peak} (keV)	L_{iso} (10^{50} erg s^{-1})	χ^2/d.o.f.	P-value	
1	XRT+BAT	129	150	SPL	2.71 ± 0.11	–	1.85 ± 0.50	–	–	58.60/45	8×10^{-2}	*
				Band	0.52	0.49 ± 0.14	2.60	$7.2^{+1.1}_{-0.9}$	0.13 ± 0.01	56.99/45	0.11	
2	XRT+BAT	150	165	SPL	2.52 ± 0.30	–	2.09 ± 0.05	–	–	166.81/101	4×10^{-5}	*
				Band	0.52	0.50	2.50 ± 0.15	$5.9^{+0.6}_{-0.5}$	0.82 ± 0.08	111.48/101	0.22	
3	XRT+BAT	165	176	SPL	2.56 ± 0.30	–	2.24 ± 0.05	–	–	161.81/91	7×10^{-6}	*
				Band	0.52	0.77	2.60 ± 0.25	$4.7^{+0.8}_{-0.6}$	0.82 ± 0.08	76.20/90	0.85	
4	XRT+BAT	176	190	SPL	1.38 ± 0.20	–	2.27 ± 0.07	–	–	105.28/85	7×10^{-2}	*
				Band	0.52	1.00	2.59 ± 0.21	$3.2^{+0.3}_{-0.3}$	0.54 ± 0.05	76.13/85	0.74	
5	XRT+BAT	190	210	SPL	1.06 ± 0.15	–	2.46 ± 0.10	–	–	64.33/88	0.97	
				Band	0.52	1.00	2.59 ± 0.16	$1.7^{+0.2}_{-0.2}$	0.35 ± 0.03	63.50/88	0.98	
6	XRT+BAT	210	224	SPL	0.82 ± 0.14	–	2.69 ± 0.13	–	–	89.96/78	0.17	
				Band	0.52	1.00	2.72 ± 0.14	< 1.01	0.17 ± 0.02	85.34/78	0.27	
7	XRT	224	249	SPL	0.88 ± 0.12	–	3.05 ± 0.13	–	–	79.94/78	0.42	
				Band	0.52	1.00	3.05 ± 0.22	< 0.4	0.087 ± 0.003	91.89/77	0.12	
8	XRT	249	320	SPL	0.71 ± 0.09	–	3.60 ± 0.18	–	–	92.80/70	0.04	
				SPL	0.52	–	3.28 ± 0.08	–	0.030 ± 0.003	105.94/71	0.01^a	

^{a}The presence of a spectral feature in excess of the SPL component in this interval of time is discussed in Margutti et al. (2008) and Moretti et al. (2008).

Table A3. Same as Table A2 for GRB 060418. A joint fit of all the spectra gives $N_{H,z} = 0.6 \pm 0.1$, χ^2/d.o.f. $= 318.43/327$, P-value $= 62$ per cent. The Galactic absorption has been frozen to 8.81×10^{20} cm^{-2} (Kalberla et al. 2005). Errors are provided at 90 per cent CL.

	Interval	t_i (s)	t_f (s)	Model	$N_{H,z}$ (10^{22} cm^{-2})	α_B	$\beta_B(\Gamma)$	E_{peak} (keV)	L_{iso} (10^{50} erg s^{-1})	χ^2/d.o.f.	P-value	
1	XRT+BAT	122	131	SPL	2.2 ± 0.50	–	2.0 ± 0.1	–	–	126.03/64	6×10^{-6}	*
				Band	0.59	0.90	2.37 ± 0.22	$5.1^{+0.9}_{-0.7}$	4.2 ± 0.4	74.26/64	0.18	
2	XRT+BAT	131	140	SPL	2.6 ± 0.4	–	2.1 ± 0.1	–	–	143.20/103	5×10^{-3}	
				Band	0.59	0.90	2.33 ± 0.13	$4.57^{+0.5}_{-0.6}$	6.6 ± 0.6	86.16/103	0.88	
3	XRT+BAT	140	148	SPL	1.91 ± 0.42	–	2.29 ± 0.12	–	–	62.85/58	0.31	
				Band	0.59	1.00	2.50 ± 0.40	$2.2^{+0.3}_{-0.4}$	2.6 ± 0.2	62.30/58	0.33	
4	XRT+BAT	148	170	SPL	1.18 ± 0.17	–	2.44 ± 0.09	–	–	96.44/107	0.76	
				Band	0.59	1.00	2.44 ± 0.11	$1.18^{+0.14}_{-0.1}$	1.0 ± 0.1	96.32/107	0.76	

This paper has been typeset from a TEX/LATEX file prepared by the author.